AFOSR-TR-97-0368

REPORT DOCUMENTATION PAGE

1. AGENCY USE ONLY (Leave Blank)	2. REPORT DATE 6/18/97	3. REPORT TYPE AND DATES COVERED 1/15/94 – 1/14/97

4. TITLE AND SUBTITLE	5. FUNDING NUMBERS
On-Line Impact Identification of Composite Structures Using Built-In Piezoelectrics	F49620-94-1-0116

6. AUTHORS

Fu-Kuo Chang and Michael J. Tracy

7. PERFORMING ORGANIZATION NAME(S) AND ADDRESS(ES)	8. PERFORMING ORGANIZATION REPORT NUMBER
Stanford University Stanford, CA 94305-4035	SPO 11899

9. SPONSORING / MONITORING AGENCY NAME(S) AND ADDRESS(ES)	10. SPONSORING / MONITORING AGENCY REPORT NUMBER
Capt. Brian Sanders, Program Manager, Structural Mechanics Air Force Office of Scientific Research (AFOSR/NA) Bolling AFB, DC 20332-8080	

11. SUPPLEMENTARY NOTES

12a. DISTRIBUTION / AVAILABILITY STATEMENT	12b. DISTRIBUTION CODE
	DISTRIBUTION STATEMENT A Approved for public release Distribution Unlimited

13. ABSTRACT (Maximum 200 words)

A method is introduced to identify an unknown impact on a composite plate. The identification includes the impact location and force time history. A distributed piezoelectric sensor array measures the plate response to the impact. An optimization technique solves the identification problem. The technique identifies the impact by comparing the calculated model response to the measured response.

The identification method was implemented in the computer code IDIMPACT. To verify the identification system, many impacts were distributed on a 36-inch by 30-inch composite plate with a distributed surface-mounted piezoelectric sensors. The code proved to be a reliable and accurate identification system. The average error in the reported impact was .56 inch, and the average error in the energy of the force reconstruction was 15%.

14. SUBJECT TERMS	15. NUMBER OF PAGES 107
19971006 048	16. PRICE CODE

17. SECURITY CLASSIFICATION OF REPORT	18. SECURITY CLASSIFICATION OF THIS PAGE	19. SECURITY CLASSIFICATION OF ABSTRACT	20. LIMITATION OF ABSTRACT

DTIC QUALITY INSPECTED 3

On-Line Damage Diagnosis of Copmposite Structures Using Built-In PiezoelectricSensors and Actuators

Capt. Brian Sanders
Director of Structural Mechanics Program
Air Force Office of Scientific Research
Bolling, Washington, DC 20331-6448

by

Fu-Kuo Chang and Michael J. Tracy
Department of Aeronautics and Astronautics
Stanford University, Stanford, CA 94305

Tel: (415) 723-3466
Fax:(415) 725-3377
E-mail: fkchang@leland.stanford.edu

Contents

List of Tables

List of Figures

List of Symbols

$\mathbf{0}$	Zero system matrix
$\mathbf{A}$	Continuous time system matrix
$\mathbf{A_{sub}}$	2×2 sbuarray of $\mathbf{A}$
$\mathbf{B}$	Continuous time system matrix
$\mathbf{B_{sub}}$	2×1 subarray of the $\mathbf{B}$ matrix
$\mathbf{C}$	Observation matrix
$\mathbf{C}_w$	Subobservation matrix for displacement
$\mathbf{C}_{xx}$	Subobservation matrix for ϵ_{xx}
$\mathbf{C}_{yy}$	Subobservation matrix for ϵ_{yy}
b	Mass variable
$\mathbf{b}$	Vector of b components
d	Thickness of the piezoelectric
d_{31}	Manufacturers constant for piezoelectric

$\mathbf{E}$	Initial energy in sensor signal
F	Frequency components of impact force
f	Impact force
D	The isotropic bending stiffness matrix
$\mathbf{D}$	The composite bending stiffness matrix
$\left.\begin{array}{l} D_{11}, D_{12}, \\ D_{22}, D_{66}, \\ D_{12}, D_{66} \end{array}\right\}$	Elements of the composite $\mathbf{D}$ matrix
g_ϵ	Conversion between voltage and strain
h	Composite plate thickness
$\mathbf{I}$	Identity matrix
i	Imaginary number
J	Figure of merit
$\bar{J}$	Modified figure of merit
$\bar{\mathbf{J}}_x$	Gradient of figure of merit
K_{mn}	System equation frequecy components
$\mathbf{K}$	Diagonal matrix with elements K_{mn}
l	Length of piezoelectric

M	Number of frequency components in x direction
m	x counter
$\bar{m}$	Mass per unit area
N	Number of frequency components in y direction
NS	Number of sensors
N_{dof}	Number of degrees of freedom
N_e	Number of points used by preprocessor
n	y counter and time counter
P	Poling direction of Piezoelectric
$\mathbf{Q}$	Weighting matrix for reconstructed force
$\mathbf{R}$	Weighting matrix for error
S_0, S_f	Weighting form initial and final conditions
s	Calculated model response
s_{exp}	Experimentally measured response
T_s	Sampling period
t	Time variable
t_{pz}	The piezoelectric thickness

V	Piezoelectric voltage
$\mathbf{V}_{exp}$	Experimental voltage from sensors
$\mathbf{W}_{zz}, \mathbf{W}_{zf},$ $\mathbf{W}_{ff},$	Variables of backward sweep
w	Out-plane-deflection of the plate
X	x domain of Fourier Transform
$\mathbf{x}$	Vector of spatial variables
$\mathbf{x}_e$	Impact location
x	x variable
x_b	Boundary coordinate
x_i	x coordinate
x_s	Sensor coordinate
Y	y domain of Fourier Transform
y	y variable
y_b	Boundary coordinate
y_j	y coordinate
y_s	Sensor coordinate
$\mathbf{z}$	State space variable

$\dot{\mathbf{z}}$	Time derivative of state space variable

Greek symbols

Δl	Change in length of the piezoelectric
δ	The delta function
ϵ_{ls}	Error in line search
$\epsilon_{xx}, \epsilon_{yy}$	strain in the x and y directions
$\epsilon'_{xx}, \epsilon'_{yy}$	strain in the transformed coordinate system
ϵ_{rr}	strain in the r direction
$\mathbf{\Phi}$	Discrete time system matrix
$\mathbf{\Phi_{sub}}$	2×2 subarray of $\mathbf{\Phi}$ matrix
$\left. \begin{array}{l} \phi_{11}, \phi_{12} \\ \phi_{21}, \phi_{22} \end{array} \right\}$	Elements of the $\mathbf{\Phi}$ matrix
$\mathbf{\Gamma}$	Discrete time system matrix
$\mathbf{\Gamma}_{sub}$	2×1 subarray of $\mathbf{\Gamma}$
γ_1, γ_2	Elements of the $\mathbf{\Gamma}$ matrix
κ	Variable to determine direction of line search
κ_m, κ_n	Frequency componenets in the x and y directions

λ	Lagrange multiplier
θ	Coordinate transformation angle
ν	The Poisson ratio
$\boldsymbol{\nu}$	Error between measured and model response
ω_{mn}	Frequency coefficients of plate response
$\boldsymbol{\omega}$	Vector of ω_{mn} coefficients
$\dot{\boldsymbol{\omega}}$	Time derivative of $\boldsymbol{\omega}$ Vector

Subscripts

i	x counter
j	y counter
p	Counter

Chapter 1

Introduction

Damage due to an external impact is a serious problem for fiber reinforced organic matrix composite structures. An impact may cause delamination or other damage to the structures. The structures may require routine inspections to insure its integrity. A system that could automatically detect and report an impact would make inspection for impact damage only necessary when an impact of significant energy is received.

Several authors have published methods to identify an impact on a plate using sensor measurements. Wu et. al. [1], [2] and [3], presented an optimization procedure to calculate the impact history of an impact at a known location on a composite plate. They used an array of strain gauges to measure the plate response. They also developed a method to select the impact location from several possibilities on an aluminum plate. However, they did not develop a complete system for locating and reconstructing an unknown impact on a composite plate.

Another way of solving the identification problem is using a neural network. Shaw [4] and Jones [5] developed a neural network based identification method and successfully found the location of a known force. The training of the neural network becomes impractical when the force history is unknown. Reconstructing an impact force history would require nearly an infinite number of training impacts.

Approaching the problem of impact identification in another way, Gunther et al [6], recorded the time of arrival of the signal at four different fiber-optic sensors and triangulated to find the non-damaging impact location. However, in practice,

using details of the signal's time of arrival is difficult. Because the wave is dispersive, the initial part of the sensor response has a low amplitude and a high frequency content. If there is noise in the sensor, it is difficult to differentiate between the arrival of the signal and the sensor noise.

A robust and accurate impact identification system for a beam was developed by Choi and Chang [7]. An optimization technique, a smoother/filter, was used to solve the inverse problem.

The smoother/filter is employed in this research. Its use is expanded to the two-dimensional impact identification problem on a composite plate. This approach will provide a robust and reliable means of identifying the impact on composite plates with clamped or free boundary conditions and noisy sensor data.

Chapter 2

Problem Statement

The problem is identification of impacts on composite plates using a distributed sensor array. The identification includes determination of the impact location and reconstruction of its force-time history. The duration of the low-mass, high-speed impact is on the order of one millisecond. The composite plates are general symmetric laminates. The sensors measure the plate's response to an impact.

Specifically, the research addresses the identification problem for the following conditions:

- The composite plate has a symmetric layup.

- The composite plate has clamped or free boundary conditions but does not have any stiffeners.

- The length and width of the composite plate are much greater than its thickness so that shear effects on plate bending are negligible.

- The impact does not cause damage to the composite.

- The impact occurs at a point. The size of the impactor is much less than the dimensions of the plate.

- The sensors are small and widely spaced so that the bending stiffness of the plate is not effected.

The identification system is introduced in Figure 1. Using the measured response of the plate and the application parameters, the identification system reports the impact location and the reconstructed force time history.

Physical Problem

Composite plate with sensor array and clamped boundaries

Unknown impact location and force time history

Development Problem

Plate response

Application parameters

Identification system

Location

F
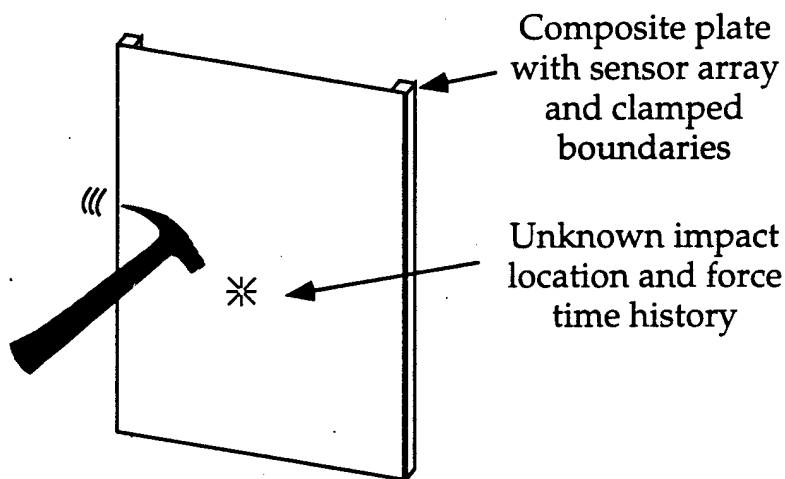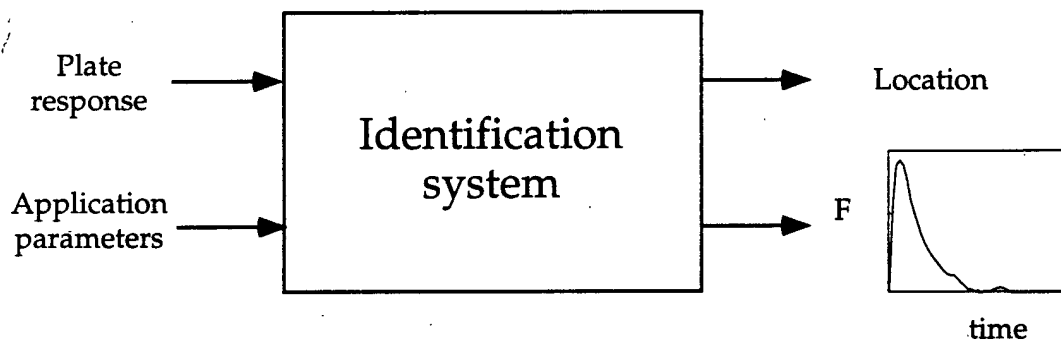
time

Figure 1: The impact identification system. The system identifies the unknown impact on the composite plate. With the plate response and application parameters, the system reports the impact location and force time history.

Chapter 3

Approach

As described in the problem statement, the identification system identifies the unknown impact on a composite plate. The input to the system is the plate response and the application parameters which describe the plate and sensor properties. The output is the impact identification which includes the impact location and force time history.

This research includes the theoretical development, the computer implementation and the experimental testing of the identification system.

The theory was developed for the four components of the identification system, see Figure 2. The sensors, the preprocessor, the forward model and the inverse problem solver.

- The plate response is measured using small circular piezoelectric sensors. The sensors measure strain where bonded to the surface of the composite plate.

- The preprocessor provides experimental data to the inverse problem solver. The preprocessor determines which sensors are closest to the impact. These sensors are isolated so that the most relevant data is used in the solution process.

- The forward model calculates the plate response as a bending wave radiating from the point of impact. The bending wave is modeled using Kirchoff's theory for composite plates. The governing equation is solved using a discrete time

integration. The model response is compared to the experimental measured response in the inverse problem solver.

- The inverse problem solver identifies an impact that will minimize the difference between the model response and the measured response. The minimization is accomplished with an outer loop estimating the impact location and an inner loop reconstructing the force history, see Figure 3. The inner loop provides a figure-of-merit that is used to update the estimated location. The procedure continues until the the best estimate of the impact location is found.

The identification system was implemented with the computer code IDIMPACT. The system runs on one machine that collects and digitizes the data and then calculates the solution. The code solves the identification problem given the digitized response of the composite plate. It reports, in a graphic interface, the impact location and force time history.

The ability of the identification program, IDIMPACT, to identify an unknown force was demonstrated on a composite plate. The system was then extensively tested with a distributed array of impacts to determine its accuracy and reliability. Finally, the robustness of the identification system was tested by introducing noise in the sensor data.

Identification system
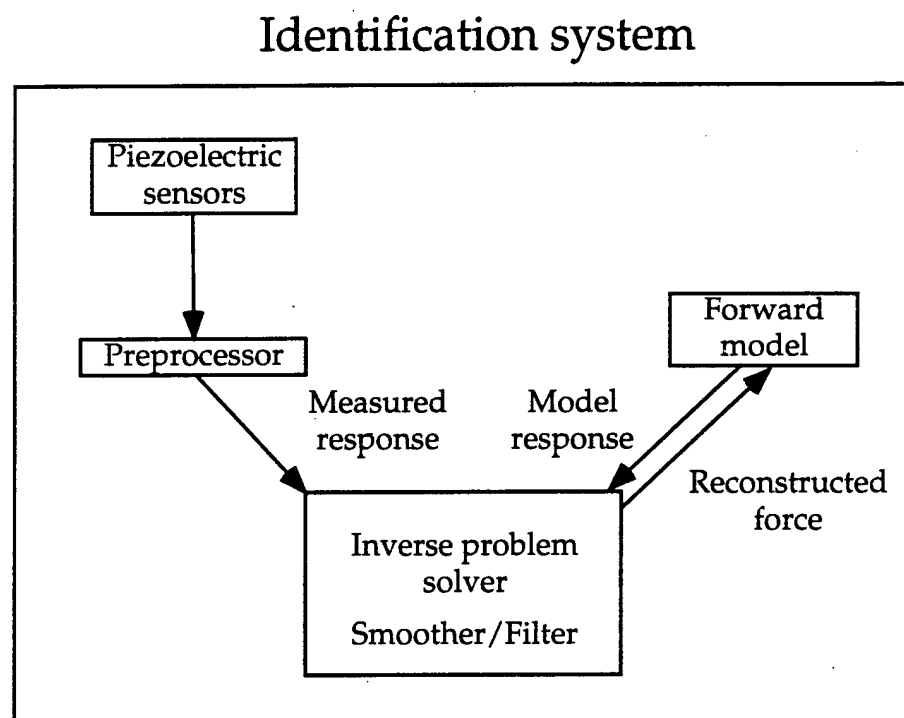
Figure 2: Inside the identification system. The sensors measure the plate response, the preprocessor isolates the relevant sensor region, and the inverse problem solver identifies the impact using the measured response and the model response.
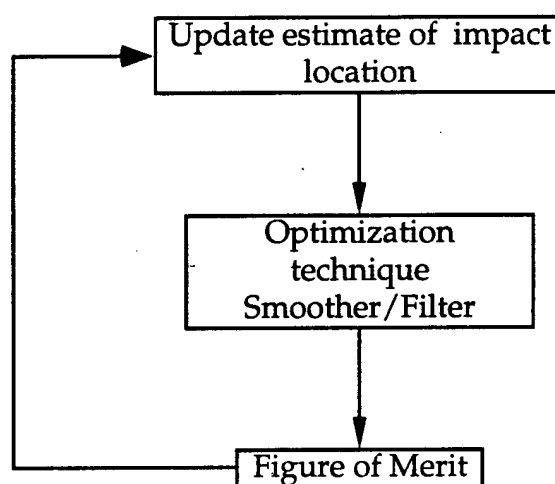
Figure 3: The inner and outer loop of the inverse problem solution.

Chapter 4

Sensor and Preprocessor

The sensors and the preprocessor provide experimental data to the inverse problem solver. Piezoelectric sensors were selected to measure the response of a composite plate to an impact. The response is digitized by the analog to digital converters. The preprocessor scans the data to find the sensors closest to the impact. The closest sensors and the corresponding area are used in the solution process.

4.1 Piezoelectric Sensors

The small circular piezoelectrics are manufactured by Piezo Kinetics Incorporated. The sensors are good for dynamic reading because they have a very fast response time and have sufficient voltage output that sophisticated amplification is not necessary.

The relation between the voltage output and the strain is supplied in the manufacturer's application notes. The one dimensional strain relation is

$$\epsilon_{xx} = \frac{\Delta l}{l} = d_{31} \frac{V}{t} \tag{4.1}$$

The strain ϵ_{xx} is the ratio of l, the length of the piezo, over Δl, the change in length. V is the voltage and t_{pz} is the thickness of the piezo. The piezoelectric constant, d_{31}, relates the mechanical strain (fractional deformation of the ceramic) to the electrical voltage. This constant is supplied by the manufacturer. The piezo is poled perpendicular to the x-y plane. See Figure 4 for an explanation of the geometry.

In this research, small circular piezoelectrics are used. The diameter, d, of the piezo is .25 inches. The thickness, t, is .01 inches. The equation to obtain voltage from a two dimensional strain field is

$$V = \frac{t}{d_{31}} \frac{1}{(1 - \nu)} \left(\epsilon_{xx} + \epsilon_{yy} \right) \tag{4.2}$$

This equation simplifies to the one-dimensional equation when the stress σ_y is set to zero. In that case, $\epsilon_{yy} = -\nu \epsilon_{xx}$, and Eq. 4.2 becomes

$$V = \frac{t}{d_{31}} \epsilon_{xx} \tag{4.3}$$

The experimental strain is attained from the experimental voltage data using

$$\mathbf{s}_{exp} = g_\epsilon \times \mathbf{V}_{exp} \tag{4.4}$$

where $\mathbf{V}_{exp}$ is the voltage data from each sensor. g_ϵ is the gain to convert the voltage to strain and includes the constants of Eq. 4.2 and the effects of bonding. This constant can be determined experimentally by comparing the forward model to the experimental data. The experimental strain, $\mathbf{s}_{exp}$, contains the experimental strain data for all the sensors.

The circular piezos measure a non-directional strain property. The combination of strain, $\epsilon_{xx} + \epsilon_{yy}$, is a two-dimensional strain invariant. The measurement is independent of the orientation of the coordinate system. This can be demonstrated using the two-dimensional strain transformation tensor where θ is the angle of coordinate rotation.

$$\begin{bmatrix} \epsilon'_{xx} \\ \epsilon'_{yy} \\ \epsilon'_{xy} \end{bmatrix} = \begin{bmatrix} \cos^2(\theta) & \sin^2(\theta) & \cos(\theta)\sin(\theta) \\ \sin^2(\theta) & \cos^2(\theta) & -\cos(\theta)\sin(\theta) \\ -2\cos(\theta)\sin(\theta) & 2\cos(\theta)\sin(\theta) & \cos^2(\theta) - \sin^2(\theta) \end{bmatrix} \begin{bmatrix} \epsilon_{xx} \\ \epsilon_{yy} \\ \epsilon_{xy} \end{bmatrix} \tag{4.5}$$

The strain combination is then

$$\epsilon'_{xx} + \epsilon'_{yy} = \epsilon_{xx} + \epsilon_{yy} \tag{4.6}$$

The quantity is not changing with the rotation of the coordinate system. By providing a non-directional means of measuring the plate response, the sensor simplifies the inverse problem solution.

The sensors used in this research measure the strain invariant $\epsilon_{xx} + \epsilon_{yy}$. The experimentally measured quantity becomes

$$s_{exp} = \epsilon_{xx} + \epsilon_{yy} \tag{4.7}$$

It is assumed that the diameter of the circular piezo is significantly smaller than the wave length of the plate response. The sensor response is calculated as a point property of strain. It is assumed the effect of averaging the experimental strain over the sensor surface area is small. This assumption will be tested in the application of the identification system by comparing the sensor diameter to the global response of the composite plate.

4.2   Preprocessor

The preprocessor selects the sensors closest to the impact location. This allows for a region of the sensor array to be isolated for the inverse problem solver.

The preprocessor scans the experimental strain to find the sensors closest to the impact. It determines the close sensors by comparing the energy in an initial time window of the data. It calculates the energy using

$$E = \sum_{i=0}^{N_e-1} s_{exp}^2(i) \tag{4.8}$$

where E is the energy of the sensors being scanned. N_e is the number of data points included in the initial time window. The number of points used should be enough that sensors close to the impact have a large energy content while those far away have close to zero.

The energy of each of the sensors are compared. The sensors with the greatest energy and the corresponding region of the plate are then used by the inverse problem solver. This method provides a method that is not susceptible to noise in the

experimental data and provides a reliable way to isolate a region of the sensor array.
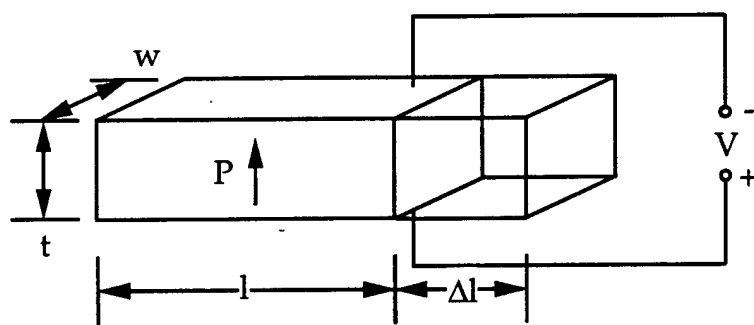
Figure 4: The description of the relationship between strain and voltage for the piezoelectric. The piezo is poled, P, in the vertical direction and strained horizontally.

Chapter 5

Forward Model

The forward model calculates the plate response as a bending wave radiating from the point of impact. The bending wave is modeled using Kirchoff's theory for composite plates. A governing equation is developed that describes the plate response, both displacement and strain, at specific points. The governing fourth-order differential equation is reduced to a system of first-order equations using a Fourier transformation. The equations are recast in state-space form and solved with a discrete-time integration. The plate can have either clamped or free boundary conditions. The model response is compared to the experimental measured response in the inverse problem solver.

The accuracy of the forward model is verified by comparison with an analytic solution of an isotropic plate and with an experimental impact on a composite plate.

5.1   Governing Equation

The governing equation for the composite plate can be expressed in state space form. Starting with Kirchoff's plate-bending theory generalized for composite plates with symmetric layups, the governing equation for a point impact is

$$
\begin{aligned}
f(t)\delta(x,y) \;=\; & D_{11}\frac{\partial^4 w}{\partial x^4} + 4D_{16}\frac{\partial^4 w}{\partial x^3 \partial y} + 2(D_{12}+2D_{66})\frac{\partial^4 w}{\partial x^2 \partial y^2} \\
& + \; 4D_{26}\frac{\partial^4 w}{\partial x \partial y^3} + D_{22}\frac{\partial^4 w}{\partial y^4} + \bar{m}\frac{\partial^2 w}{\partial t^2}
\end{aligned}
\tag{5.1}
$$

$f(t)\delta(x,y)$ is the point load located at $(0,0)$, D_{ij} are elements of the composite laminate matrix $\mathbf{D}$, (Tsai [8]), and w is the out-of-plate deflection of the plate.

This governing equation is applied to an infinite plate by using the two-dimensional discrete Fourier transformation with respect to the spatial variables x and y.

$$
w(x_i,y_j,t) = \sum_{n=0}^{N-1}\sum_{m=0}^{M-1} \bar{\omega}_{mn}(\kappa_m,\kappa_n,t)e^{i\kappa_m x_i + i\kappa_n y_j}
\tag{5.2}
$$

The frequency components are calculated using $\kappa_m = \frac{2\pi m}{X}$ and $\kappa_n = \frac{2\pi n}{Y}$. X and Y are the extent of the spatial domain. $\bar{w}_{mn}$ is the amplitude of each frequency component. Applying the transform to both sides of the equation yields the component equation

$$
\begin{aligned}
& (D_{11}\kappa_m^4 + 4D_{16}\kappa_m^3\kappa_n + 2(D_{12}+2D_{66})\kappa_m^2\kappa_n^2 + \\
& 4D_{26}\kappa_m\kappa_n^3 + D_{22}\kappa_n^4)\,\bar{\omega}_{mn} + \bar{m}\frac{\partial^2 \bar{\omega}_{mn}}{\partial t^2} = f(t)
\end{aligned}
\tag{5.3}
$$

These component equations can be regrouped by introducing the state-space formulation.

$$
\frac{\partial}{\partial t}\begin{bmatrix} \bar{w}_{mn} \\ \dot{\bar{w}}_{mn} \end{bmatrix} = \begin{bmatrix} 0 & 1 \\ -K_{mn} & 0 \end{bmatrix}\begin{bmatrix} \bar{w}_{mn} \\ \dot{\bar{w}}_{mn} \end{bmatrix} + \begin{bmatrix} 0 \\ b \end{bmatrix}f(t)
\tag{5.4}
$$

where

$$K_{mn} = \frac{1}{\bar{m}} \left(D_{11}\kappa_m^4 + 4D_{16}\kappa_m^3\kappa_n + 2(D_{12} + 2D_{66})\kappa_m^2\kappa_n^2 \right.$$
$$\left. + 4D_{26}\kappa_m\kappa_n^3 + D_{22}\kappa_n^4 \right) \tag{5.5}$$

and

$$b = \frac{1}{\bar{m}} \tag{5.6}$$

This state-space formulation is completed when the terms are collected to generate the system equation in matrix form.

$$\dot{z} = \frac{\partial}{\partial t}\begin{bmatrix} \bar{\omega} \\ \dot{\bar{\omega}} \end{bmatrix} = \begin{bmatrix} 0 & I \\ K & 0 \end{bmatrix}\begin{bmatrix} \bar{\omega} \\ \dot{\bar{\omega}} \end{bmatrix} + \begin{bmatrix} 0 \\ b \end{bmatrix} f(t) \tag{5.7}$$
$$\equiv Az + Bf(t)$$

I is an $[N \cdot M \times N \cdot M]$ identity matrix, **0** is a zero matrix of the same size, **b** and $\bar{\omega}$ are $[N \cdot M \times 1]$ vectors with the elements

$$\mathbf{b}(n + Nm) = \frac{1}{\bar{m}} = b \tag{5.8}$$

$$\bar{\omega}(n + Nm) = \bar{\omega}_{mn} \tag{5.9}$$

and **K** is a diagonal matrix, $[N \cdot M \times N \cdot M]$, with the diagonal elements

$$\mathbf{K}(n + Nm, n + Nm) = K_{mn} \tag{5.10}$$

where $m = 0, \ldots, (M-1)$ and $n = 0, \ldots, (N-1)$

5.2 Plate Response

A state space formulation is used to calculate the plate response. The Fourier Transform provides the out-of-plane deflection of the composite plate at $x = x_i$ and $y = y_j$

$$w(x_i, y_j, t) = \sum_{n=0}^{N-1} \sum_{m=0}^{M-1} \bar{\omega}_{mn}(\kappa_m, \kappa_y, t) e^{i\kappa_m x_i + i\kappa_n y_j} \qquad (5.11)$$

The equation can be represented in matrix form. $\bar{\omega}$ is a $[1 \times N \cdot M]$ vector. A vector with $[N \cdot M \times 1]$ elements is defined for the exponential terms. For $m = 0, \ldots, (M-1)$ and $n = 0, \ldots, (N-1)$

$$\mathbf{C}_w(n + Nm) = e^{i\kappa_m x_i + i\kappa_n y_j} \qquad (5.12)$$

The calculation of the displacement becomes

$$w(x_i, y_i, t) = \mathbf{C}_w \bar{\omega} \qquad (5.13)$$

A more general form of this equation can be defined

$$\mathbf{s} = \mathbf{C}\mathbf{z} \qquad (5.14)$$

where $\mathbf{s}$ is the general measured quantity - displacement, acceleration or strain. $\mathbf{s}$ is a $[NS \times 1]$ vector where NS is the number of sensors in the system. Each element of $\mathbf{s}$ is the response of one sensor at time step n. The $\mathbf{C}$ matrix, is the observation matrix. For one sensor

$$\mathbf{C} = \begin{bmatrix} \mathbf{C}_w & \mathbf{0} \end{bmatrix} \qquad (5.15)$$

$\mathbf{C}$ is a $[NS \times N \cdot M]$ matrix where each row represents one sensor.

The observation matrix can be simplified using the symmetry of the impact problem and the properties of a Fourier transformation for real and even functions, see Appendix A. The simplified submatrix becomes a $\left[NS \times (\frac{N}{2} + 1) \cdot (\frac{M}{2} + 1)\right]$ matrix. For $m = 0, \ldots, \frac{M}{2}$ and $n = 0, \ldots, \frac{N}{2}$, each row becomes

$$\mathbf{C}_w =$$

$$[\qquad 1 \quad \cdots \quad 2\cos(\kappa_n y_j) \qquad \cdots \qquad \cos(\kappa_{N/2} y_j)$$

$$\cdots \quad 2\cos(\kappa_m x_i) \quad \cdots \quad 4\cos(\kappa_m x_i)\cos(\kappa_n y_j) \quad \cdots \quad 2\cos(\kappa_m x_i)\cos(\kappa_{N/2} y_j)$$

$$\cdots \quad \cos(\kappa_{M/2} x_i) \quad \cdots \quad 2\cos(\kappa_{M/2} x_i)\cos(\kappa_n y_j) \quad \cdots \quad \cos(\kappa_{M/2} x_i)\cos(\kappa_{N/2} y_j) \quad]$$

$$(5.16)$$

5.3 Strain Measurement

Strain is often the measured quantity in structures applications. To calculate strain with the measured quantity $\mathbf{s}(t)$, an appropriate strain observation matrix is required.

The equations for surface strain are

$$
\begin{aligned}
\epsilon_{xx}(x_i, y_j, t) &= -\frac{h}{2}\frac{\partial^2 w}{\partial x^2} \\
&= \frac{h}{2}\sum_{n=0}^{N-1}\sum_{m=0}^{M-1}\kappa_m^2 \bar{w}_{mn} e^{i\kappa_m x_i + i\kappa_n y_j}
\end{aligned}
$$

$$(5.17)$$

$$
\begin{aligned}
\epsilon_{yy}(x_i, y_j, t) &= -\frac{h}{2}\frac{\partial^2 w}{\partial y^2} \\
&= \frac{h}{2}\sum_{n=0}^{N-1}\sum_{m=0}^{M-1}\kappa_n^2 \bar{w}_{mn} e^{i\kappa_m x_i + i\kappa_n y_j}
\end{aligned}
$$

where h is the thickness of the plate, ϵ_{xx} is the strain measured on the surface of the plate in the x direction, and ϵ_{yy} is the strain in the y direction.

Similar to displacement, the strain equations can be written in matrix form. The strain equations become

$$\epsilon_{xx}(x_i, y_j, t) = \mathbf{C}_{xx}\bar{\omega} \qquad (5.18)$$

$$\epsilon_{yy}(x_i, y_j, t) = \mathbf{C}_{yy}\bar{\omega} \tag{5.19}$$

The elements of the the strain submatrices $\mathbf{C}_{xx}$ and $\mathbf{C}_{yy}$ are

$$\begin{aligned}
(\mathbf{C}_{xx})(n + Nm) &= \kappa_m^2 (\mathbf{C}_w)(n + Nm) \\
(\mathbf{C}_{yy})(n + Nm) &= \kappa_n^2 (\mathbf{C}_w)(n + Nm)
\end{aligned} \tag{5.20}$$

where $m = 0, \ldots, (M - 1)$ and $n = 0, \ldots, (N - 1)$.

The general measured quantity $\mathbf{s}(t)$ can now be used to calculate the strain. Although the observation equation remains unchanged,

$$\mathbf{s}(t) = \mathbf{C}\mathbf{z} \tag{5.21}$$

the observation submatrix has changed. For each sensor measuring strain in the x direction and

$$\mathbf{C} = \begin{bmatrix} \mathbf{C_{xx}} & \mathbf{0} \end{bmatrix} \tag{5.22}$$

and for each sensor measuring in the y direction

$$\mathbf{C} = \begin{bmatrix} \mathbf{C_{yy}} & \mathbf{0} \end{bmatrix} \tag{5.23}$$

5.4 Discrete Time Domain

To solve the governing equation, the state-space formulation developed in the previous section is converted to the discrete time domain. The system formulation in the continuous time domain is

$$\dot{\mathbf{z}} = \mathbf{A}\mathbf{z} + \mathbf{B}f(t) \tag{5.24}$$

$$\mathbf{s}(t) = \mathbf{C}\mathbf{z} \tag{5.25}$$

In the discrete time domain, the governing equations become

$$\mathbf{z}(n+1) = \begin{bmatrix} \phi_{11} & \phi_{12} \\ \phi_{21} & \phi_{22} \end{bmatrix} \mathbf{z}(n) + \begin{bmatrix} \gamma_1 \\ \gamma_2 \end{bmatrix} f(n) \tag{5.26}$$

$$\equiv \mathbf{\Phi}\mathbf{z}(n) + \mathbf{\Gamma}f(n)$$

and the observation equation becomes

$$\mathbf{s}(n) = \mathbf{C}\mathbf{z}(n) \tag{5.27}$$

where $n = 0, \ldots, (NT - 1)$. The new matrices are defined as

$$\mathbf{\Phi} = \exp(\mathbf{A}T_s) \tag{5.28}$$

$$\mathbf{\Gamma} = \int_0^{T_s} \exp(\mathbf{A}t)dt\,\mathbf{B} \tag{5.29}$$

See Franklin, et. al. [9] for a discussion of these relations. $\mathbf{\Phi}$ is a block diagonal matrix. ϕ_{11} through ϕ_{22} are $[N \cdot M \times N \cdot M]$ diagonal matrices. γ_1 and γ_1 are $[N \cdot M \times 1]$ vectors. The observation matrix $\mathbf{C}$ remains unchanged.

The solution to the discrete time equations begins with an initial condition, $\mathbf{z}(0)$ and the initial value of the force $f(0)$. The variables are calculated at the discrete time step n where the time is $t = nT_s$. T_s is the sampling period. If the plate is initially at rest, $\mathbf{z}(0) = 0$. The time history of the strain is constructed by calculating $\mathbf{z}(n+1)$ from $\mathbf{z}(n)$ and $f(n)$ and updating the measured quantity $\mathbf{s}(n)$.

The discrete time relations, Eq. 5.28 and Eq. 5.29, can be solved to facilitate the numeric implementation. Defining $\mathbf{A}_{sub}$, a 2×2 subarray of the $\mathbf{A}$ matrix,

$$\mathbf{A}_{sub} = \begin{bmatrix} 0 & 1 \\ -\mathbf{K}(n+Nm, n+Nm) & 0 \end{bmatrix} \tag{5.30}$$

a subarray $\boldsymbol{\Phi}_{sub}$ of the $\boldsymbol{\Phi}$ matrix can be calculated using Eq. 5.28. For n and $m \neq 0$, the resulting $\boldsymbol{\Phi}$ subarray is

$$
\begin{aligned}
\boldsymbol{\Phi}_{sub} &= \begin{bmatrix} \phi_{11}(n+Nm) & \phi_{12}(n+Nm) \\[1em] \phi_{21}(n+Nm) & \phi_{22}(n+Nm) \end{bmatrix} \\
&= \begin{bmatrix} \cos\left(T_s\sqrt{K_{mn}}\right) & \dfrac{1}{\sqrt{K_{mn}}}\sin\left(T_s\sqrt{K_{mn}}\right) \\[1em] \sqrt{K_{mn}}\sin\left(T_s\sqrt{K_{mn}}\right) & \cos\left(T_s\sqrt{K_{mn}}\right) \end{bmatrix}
\end{aligned}
\tag{5.31}
$$

Similarly, defining $\mathbf{B}_{sub}$ as a subarray of the $\mathbf{B}$ matrix, the elements of the $\boldsymbol{\Gamma}$, $\boldsymbol{\Gamma}_{sub}$, can be calculated using Eq. 5.29. The $\mathbf{B}$ subarray is

$$
\mathbf{B}_{sub} = \begin{bmatrix} 0 \\ b \end{bmatrix}
\tag{5.32}
$$

and, for n and $m \neq 0$, the resulting $\boldsymbol{\Gamma}$ subarray is

$$
\boldsymbol{\Gamma}_{sub} = \begin{bmatrix} \phi_1(n+Nm) \\[1em] \phi_2(n+Nm) \end{bmatrix} = \begin{bmatrix} -\dfrac{b}{K_{mn}}\cos\left(T_s\sqrt{K_{mn}}\right) + \dfrac{b}{K_{mn}} \\[1em] \dfrac{b}{\sqrt{K_{mn}}}\sin\left(T_s\sqrt{K_{mn}}\right) \end{bmatrix}
\tag{5.33}
$$

If m and $n = 0$, then

$$
\boldsymbol{\Phi}_{sub} = \begin{bmatrix} 1 & T_s \\ 0 & 1 \end{bmatrix}
\tag{5.34}
$$

$$
\boldsymbol{\Gamma}_{sub} = \begin{bmatrix} b\dfrac{T_s^2}{2} \\[1em] bT_s \end{bmatrix}
\tag{5.35}
$$

5.5 Forward Model Verification

To verify the accuracy of the forward model response, it was compared to an analytic solution of an isotropic plate and the measured response of a composite plate.

The analytical solution for an isotropic aluminum plate is presented in Doyle [10]. The strain response is calculated in radial coordinates using the Fourier Transform

$$\epsilon_{rr}(k) = \frac{1}{N} \sum_{j=0}^{N-1} \hat{\epsilon}_{rr}(j) e^{\frac{-2\pi ijk}{N}} \tag{5.36}$$

where

$$\hat{\epsilon}_{rr}(j) = \frac{iF(j)h}{32D} \left[(J_0 - J_2) - i(Y_0 - Y_2) + \frac{i2}{\pi}(K_0 - K_2) \right] \tag{5.37}$$

and

$$F(j) = \sum_{p=0}^{N-1} f(p) e^{\frac{-2\pi ijp}{N}} \tag{5.38}$$

f is the force time history. D is the bending stiffness of the isotropic plate. i is equal to $\sqrt{-1}$. The argument for the Bessel functions J, Y and K, is

$$z = \beta r \qquad \beta = \sqrt{\omega} \left[\frac{\rho h}{D} \right]^{1/4} \tag{5.39}$$

where ρ is the density of the isotropic material.

A half-sine-wave impact was the input to the forward model and the analytic solution. The responses are compared in Figure 5. A very small error was seen to accrue in the forward model.

The forward model was also compared to the measured response from an actual impact on composite plate. A T800 composite plate with a $[45/90/-45/0_2/45/0_2/-45/0]_s$ layup and clamped boundaries was used. The composite **D** matrix for the plate is

$$D = \begin{bmatrix} 2265.4 & 641.6 & 185.1 \\ 641.6 & 1990.2 & 185.1 \\ 185.1 & 185.1 & 760.6 \end{bmatrix} \tag{5.40}$$

where the units are lbs-in. The mass per unit area of the plate, $\bar{m}$ is .000165 lb s^2/ft^3. The plate is 30" x 36". The thickness of each ply is .007 inches for a total thickness is .14 inches.

The response was calculated with Eq. 5.26 and Eq. 5.27 where $N = M = 180$, $NT = 45$, $T_s = 4.48 \times 10^{-5}$ seconds, and $X = Y = 90$ inches.

The plate was hit at its center and the strain response was measured at four locations. The plate dimensions, sensors coordinates and boundaries are shown in Figure 6. The sensors were located along the 45 degree ply direction and the 90 degree ply direction. The sensors at different ply directions test if the model includes the anisotropic properties of the plate. ·

The impact force was recorded using an instrumented hammer. The hammer was manufactured by PCB Piezotronics. It has a 208 A04 force transducer and a 480A power unit. The impact force history is shown in Figure 7. The model response to this impact is compared to the experimental response in Figure 8 and Figure 9. The forward model was shown to be a simple and reasonable means of calculating the impact response of the plate.

5.6 Boundaries

In real-life applications the plate will have boundaries. The effects of the boundaries can be approximated by adding mirror images of the actual impact about the boundaries.

A sensor bonded to an actual plate with boundaries measures the initial wave generated by the impact and the wave after it has reflected from the boundaries. In the forward model, the effect of these boundaries can be simulated by adding the infinite plate solution with the impact located symmetrically about the boundaries. The sensor in the forward model then includes the response from the impact as well as the response from the image impacts. The sum of the impact responses approximate the effect of the plate boundary.

The location of the image impacts to simulate the first reflection from each of the four boundaries is shown in Figure 10. The location of the boundary is measured
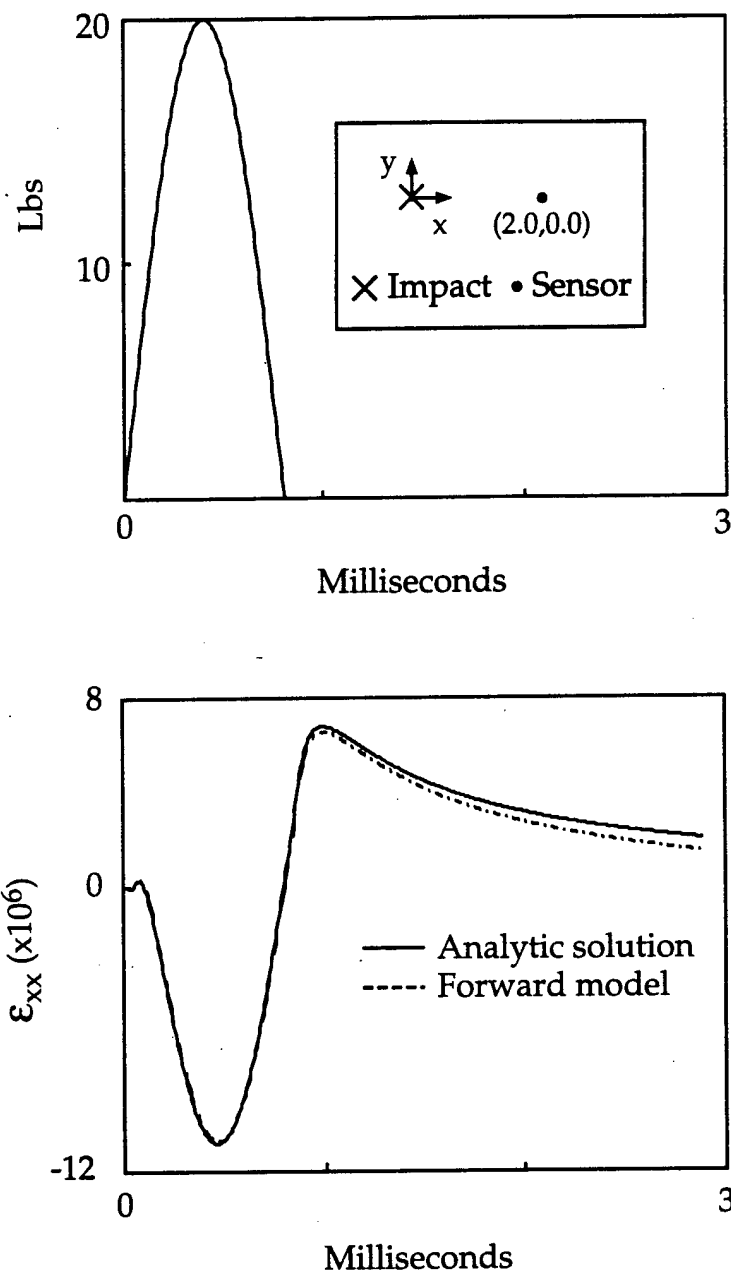
Figure 5: Comparison of the forward model and the analytic solution. The response of an isotropic plate to a half sine wave impact is calculated using the forward model and the analytic solution. The location of the sensor relative to the impact is shown. A very small error accrues in the forward model.
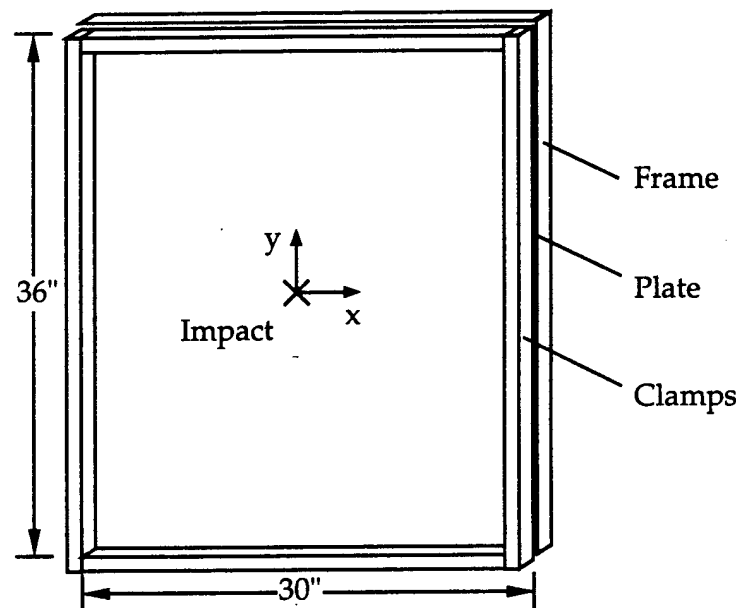
Figure 6: The experimental setup to verify the forward model. The zero ply direction is in the x direction.
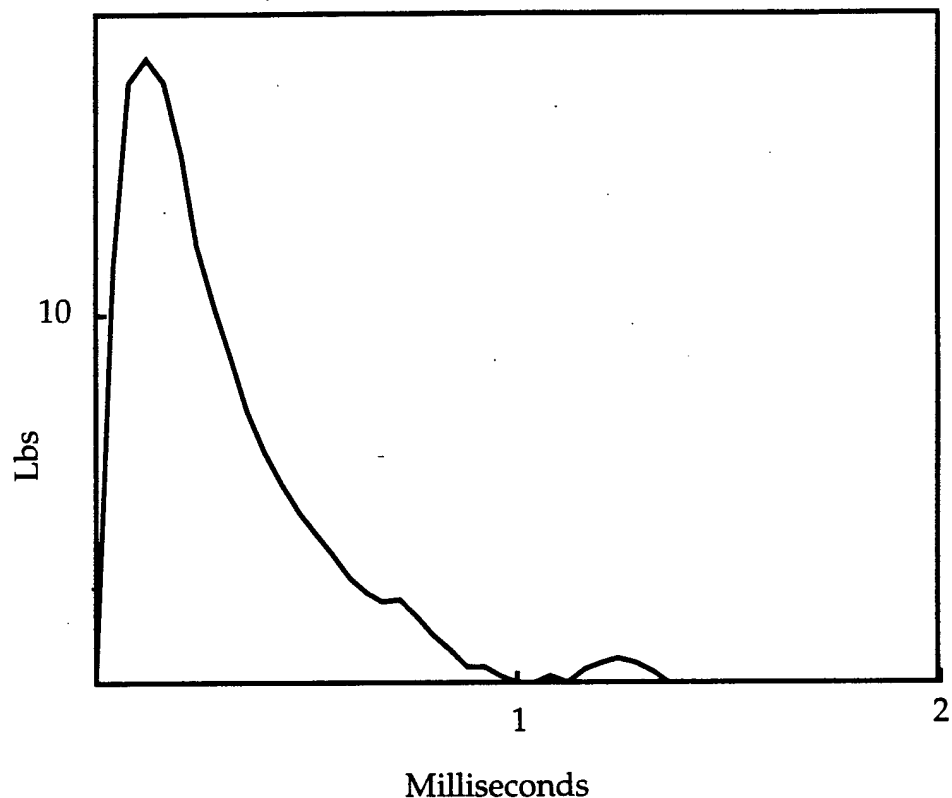
Figure 7: Experimentally recorded impact. This impact was used to compare the forward model response and the experimental response. The x-axis is the zero ply direction.
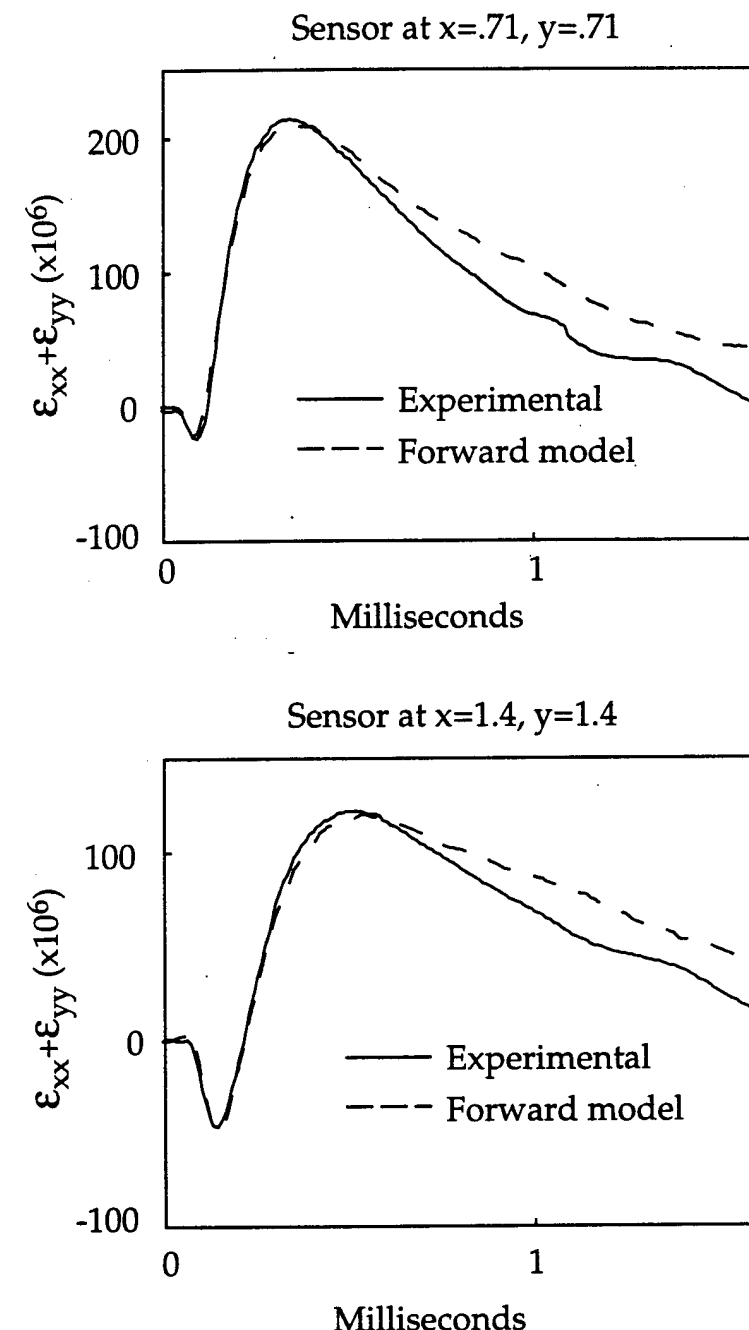
Figure 8: Verification of the forward model. The graphs compare the model response to the experimental response at two locations.
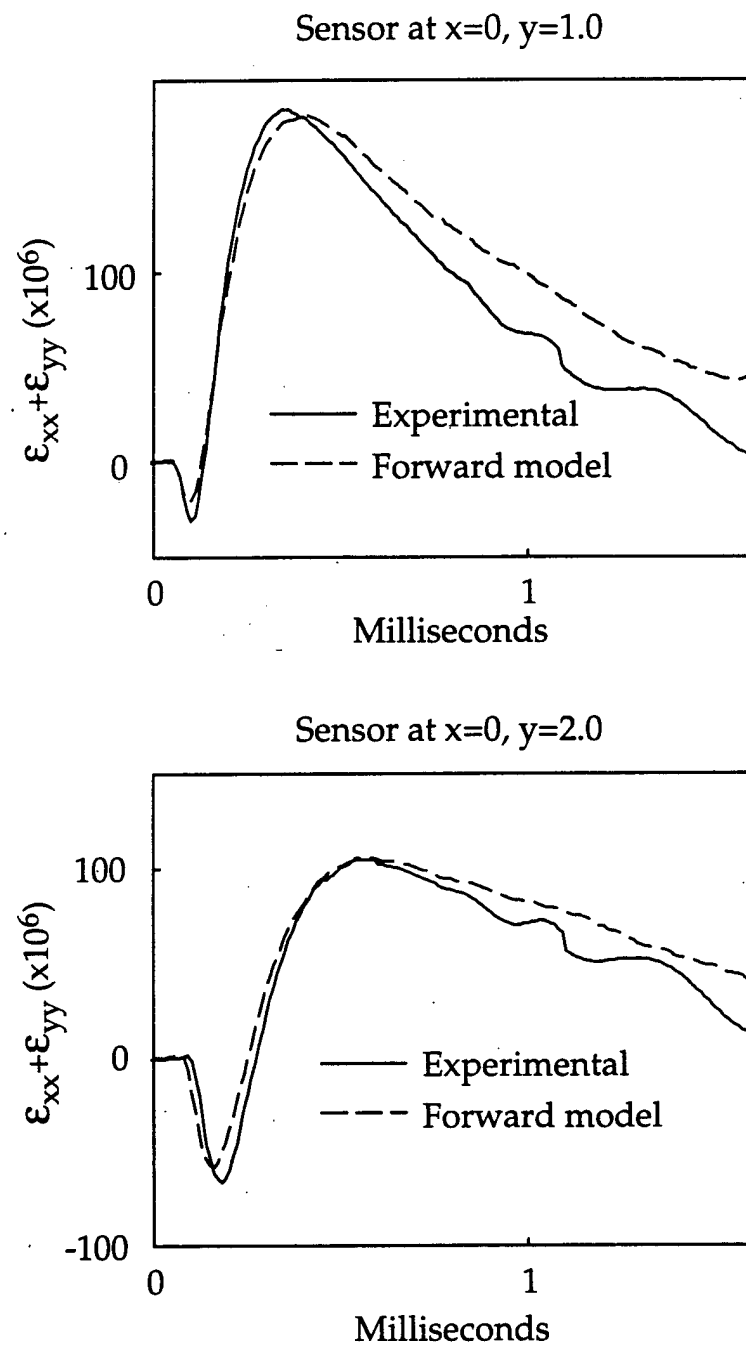
Figure 9: Verification of Composite Plate Model

perpendicular from the impact location. Image impacts can also be added to simulate second and third reflections.

In the forward model, only the observation matrix is affected. The **C** matrix is the summation of the observation matrices translated to the correct point relative to each image impact. The observation matrix for the first reflection from the clamped boundaries is

$$\mathbf{C} = \mathbf{C}(x_s, y_s) + \mathbf{C}(x_s - 2x_{b_n}, y_s - 2y_{b_n}) \qquad (5.41)$$

where (x_{b_n}, y_{b_n}) is the location of the boundary measured perpendicular from the impact location. There are a set of coordinates for each boundary, so $n = 0, \ldots, (Nb - 1)$ and Nb is the number of boundaries. For free boundary conditions

$$\mathbf{C} = \mathbf{C}(x_s, y_s) - \mathbf{C}(x_s - 2x_{b_n}, y_s - 2y_{b_n}) \qquad (5.42)$$

where the only difference is the sign of the image impact.

The forward model with the image impact is compared to the measured response in Figure 11. The impact and sensor were located so there was significant boundary effect in the signal. The impact was near the center of the plate, 12.5 inches from right clamped boundary and 20 inches from the top. The sensor was located 5 inches from the right boundary and 25 inches form the top. With the sensor further away from the impact, the match between the model and the measured response is not as close as in Figure 8 and Figure 9. The general shape of the response is present but some of the higher frequency reflected waves are not well modeled.

5.7 Global Response

The impact response of the entire plate can be calculated at one point in time. At every point in the space domain Eq. 5.21 is used to calculate the plate deflection.
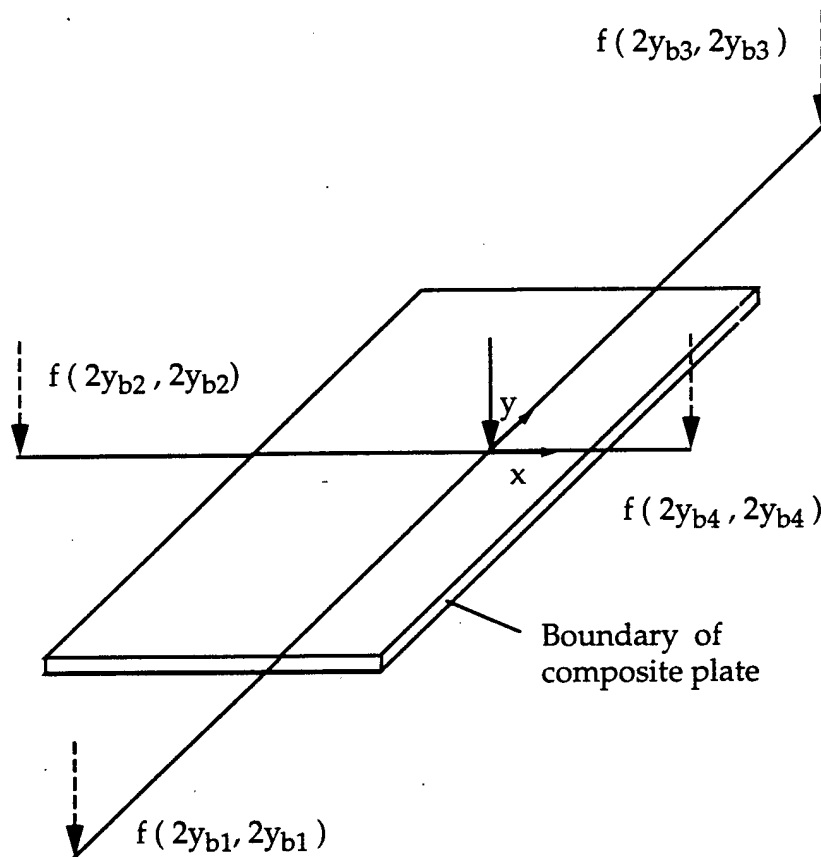
Figure 10: Simulation of clamped boundaries. The boundaries of the real plate are simulated using image impacts. The image and the actual impact are located symmetrically about the boundaries.
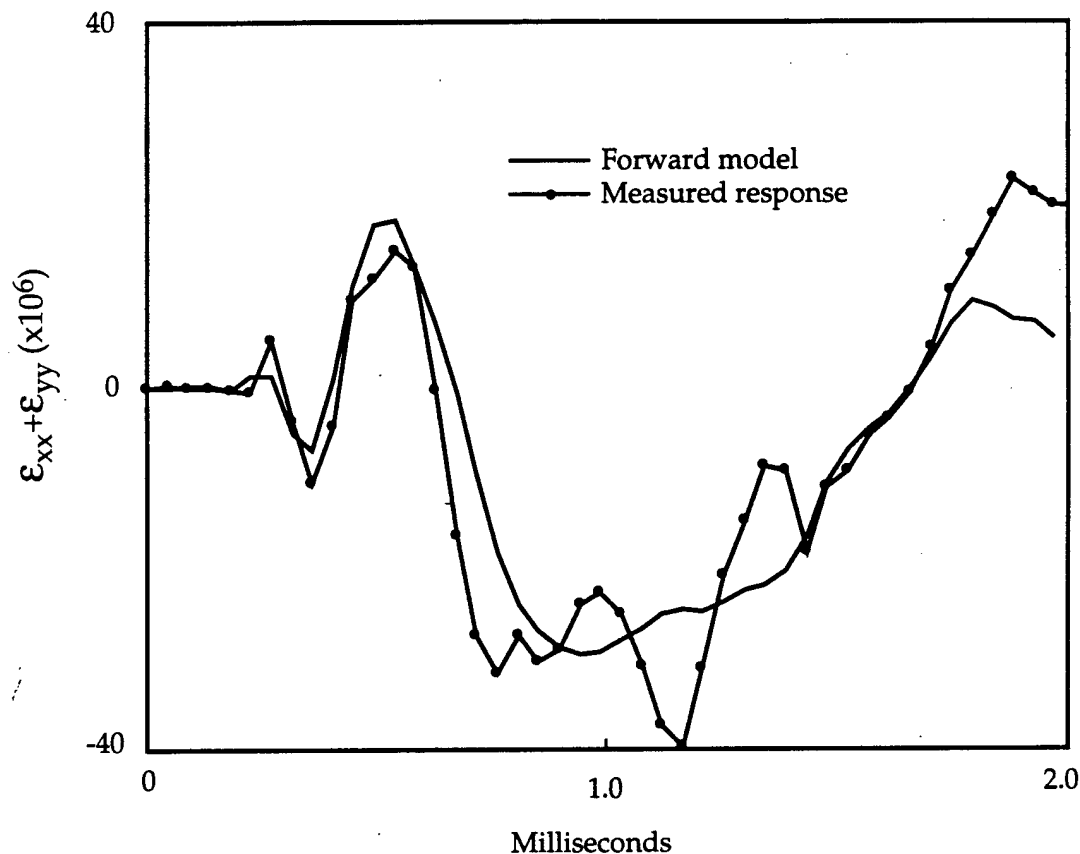
Figure 11: Verification of the forward model where there is significant bound-
ary effect. The sensor is 5 inches from the right clamped boundary
and 25 inches form the top. The impact is 12.5 inches from the
right boundary and 20 inches from the top.

The force time history of Figure 7 was applied to the center of the composite plate. The response at time step $n = 22$ or $t = .986$ milliseconds is shown in Figure 12.

From the global response, it is evident that the wavelength of the response is several inches. With this wave length, the assumption of the sensors measuring a point property of the strain appears reasonable.
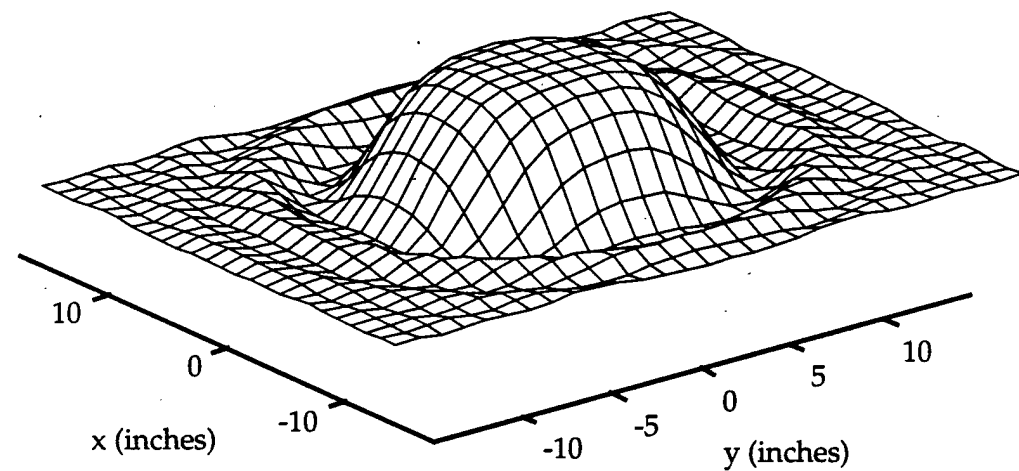
Figure 12: The global response of the $T800$ composite plate. The plate with clamped boundaries is hit in the middle. The displacement is calculated at time step $n = 22$ or $t = .986$ milliseconds.

Chapter 6

Inverse Problem Solver

The inverse problem solver is the key component of the identification system. The solver identifies an impact that will minimize the difference between the model response and the measured response.

The solution to the inverse problem has two major elements. The outer loop searches for the impact location and the inner loop, the smoother/filter, reconstructs the impact force time history. The solution starts from the outer loop with an estimate of the impact location. At this location the filter/smoother reconstructs a force history. The solution continues when the figure-of-merit, based on the difference between the model response and the experimental response, is reported to the outer loop and is used to improve the estimate of the impact location.

6.1 The Inner Loop - The Smoother/Filter

At an estimated impact location, the smoother/filter reconstructs a force history based on the experimental response. This technique of using the system response to find the system properties and the unknown input was presented by Bryson [11]. The technique successfully found system properties of a helicopter using flight test data. The following development closely follows Bryson's method.

The reconstruction of the force history begins with the definition of the figure-of-merit.

$$J = \frac{1}{2}[\mathbf{z}_0 - \mathbf{z}(0)]^T \mathbf{S}_0 [\mathbf{z}_0 - \mathbf{z}(0)] + \frac{1}{2}\sum_{n=0}^{NT-1} f(n)\mathbf{Q}f(n)$$
$$+ \frac{1}{2}\sum_{n=0}^{NT-1} \boldsymbol{\nu}^T(n)\mathbf{R}\boldsymbol{\nu}(n) + \frac{1}{2}[\mathbf{z}_{NT} - \mathbf{z}(NT)]^T \mathbf{S}_f [\mathbf{z}_{NT} - \mathbf{z}(NT)] \tag{6.1}$$

where $\mathbf{z}_0$ and $\mathbf{z}_{NT}$ are user-supplied guesses of initial and final states. f is the reconstructed force. $\boldsymbol{\nu}$ is the error between the experimental data, $\mathbf{s}_{exp}$, and the model response, $\mathbf{s}$. The error contains both the effects of measurement noise and the error due to incorrect estimation of the impact. $\mathbf{Q}$ is the diagonal weighting matrix for the input force and $\mathbf{R}$ for the states. $\mathbf{S}_0$ and $\mathbf{S}_f$ are weighting matrices for the initial and final conditions.

The values $\mathbf{Q}$ and $\mathbf{R}$ were set to .05 and 5.0×10^{10}. These values were based on Choi's [12] work on the beam and were adjusted empirically for the composite plate. Additional information on these values can be found in Sage and Melsa [13]. The system is at rest prior to the impact so $\mathbf{z}_0$ is set to zero and $\mathbf{S}_0$ is set to a very high value. Since the final condition is unpredictable, $\mathbf{S}_f$ is set to zero.

The objective is to minimize J. This means that the error, $\boldsymbol{\nu}$, is minimized, the force reconstruction, f, is constrained and the initial conditions are constrained. The force is unknown but its reconstruction is constrained by penalizing J for large force values. Similarly, J is penalized when the initial condition is not met.

The minimization of the figure-of-merit is subject to the system equations of Chapter 5, Eq. 5.26 and Eq. 5.27. For $n = 0, \ldots, (NT-1)$

$$\mathbf{z}(n+1) = \boldsymbol{\Phi}\mathbf{z}(n) + \boldsymbol{\Gamma}f(n) \tag{6.2}$$

$$\mathbf{s}(n) = \mathbf{C}\mathbf{z}(n) \tag{6.3}$$

where NT is the number of time steps.

To satisfy these equations, the figure-of-merit is modified to accommodate the constraints using Lagrange multipliers $\boldsymbol{\lambda}$

$$\bar{J} = J + \sum_{n=0}^{NT-1} \lambda^T(n+1)\left[\Phi z(n) + \Gamma f(n) - z(n+1)\right] \tag{6.4}$$

where the Lagrange multiplier was introduced at an extra time step, $n = NT$. For simplicity, $\lambda(NT)$ is set equal to zero.

Minimizing $\bar{J}$ is equivalent to minimizing J subject to the constraint equations. Taking a variation on the modified figure of merit gives

$$\delta\bar{J} = \sum_{n=0}^{NT} \frac{\partial\bar{J}}{\partial z(n)}\delta z(n) + \sum_{n=0}^{NT-1} \frac{\partial\bar{J}}{\partial f(n)}\delta f(n) + \frac{\partial\bar{J}}{\partial x}\delta x \tag{6.5}$$

where x is the spatial variable

$$x = \begin{bmatrix} x \\ y \end{bmatrix} \tag{6.6}$$

At a stationary point of $\bar{J}$, the first variation vanishes for arbitrary variation of $\delta z(n)$, $\delta f(n)$ and δx, and so the coefficients of each term must vanish. The first two coefficients are solved with the smoother/filter while the third coefficient is left to the outer loop. The first coefficient is

$$\frac{\partial\bar{J}}{\partial z(n)} = \begin{cases} [z_0 - z(0)]^T S_0 + \lambda^T(1)\Phi & \text{for } n = 0 \\ -\nu^T(n)RC + \lambda^T(n+1)\Phi - \lambda^T(n) & \text{for } n = 1, \ \dots, \ NT \end{cases} \tag{6.7}$$

The second coefficient is

$$\frac{\partial\bar{J}}{\partial f(n)} = f^T(n)Q + \lambda^T(n+1)\Gamma \qquad \text{for} \quad n = 0, \ \dots, \ (NT-1) \tag{6.8}$$

Setting these two coefficients equal to zero and incorporating the system equations leads to the smoothing problem for a given x.

$$\begin{aligned} z(n+1) &= \Phi z(n) + \Gamma f(n) \\ \lambda(n) &= \Phi^T\lambda(n+1) - C^T R\nu(n) \\ f(n) &= -Q^{-1}\Gamma^T\lambda(n+1) \end{aligned} \tag{6.9}$$

The boundary conditions are

$$\mathbf{z}(0) = \mathbf{z}_0 - \mathbf{S}_0^{-1}\mathbf{\Phi}^T\boldsymbol{\lambda}(1)$$

$$\boldsymbol{\lambda}(NT) = 0 \tag{6.10}$$

This is a two-point boundary value problem. Half of the boundary conditions are given at the initial point, the other half at the final point. The boundary value problem can be solved by the sweep method. The final boundary condition may be swept backward, and the initial condition swept forward.

The boundary condition at $n = NT$ suggests a backward sweep solution of the form

$$\boldsymbol{\lambda}(n) = \mathbf{S}^B(n)\mathbf{z}(n) - \boldsymbol{\lambda}^B(n) \tag{6.11}$$

The proper form of $\mathbf{S}^B$ and $\boldsymbol{\lambda}^B$ need to be found to solve this problem. Using the following equation, $\mathbf{z}(n+1)$ can be eliminated from Eq. 6.9.

$$\begin{bmatrix} \boldsymbol{\lambda}(n) \\ 0 \end{bmatrix} = \begin{bmatrix} \mathbf{C}^T\mathbf{R}\mathbf{C} + \mathbf{W}_{zz} & \mathbf{W}_{zf} \\ \mathbf{W}_{zf}^T & \mathbf{W}_{ff} \end{bmatrix} \begin{bmatrix} \mathbf{z}(n) \\ \mathbf{f}(n) \end{bmatrix} - \begin{bmatrix} \mathbf{\Phi}^T \\ \mathbf{\Gamma}^T \end{bmatrix} \boldsymbol{\lambda}(n+1) - \begin{bmatrix} \mathbf{C}^T\mathbf{R} \\ 0 \end{bmatrix} \boldsymbol{\nu}(n) \tag{6.12}$$

where

$$\begin{bmatrix} \mathbf{W}_{zz} & \mathbf{W}_{zf} \\ \mathbf{W}_{zf}^T & \mathbf{W}_{ff} \end{bmatrix} = \begin{bmatrix} 0 & 0 \\ 0 & \mathbf{Q} \end{bmatrix} + \begin{bmatrix} \mathbf{\Phi}^T \\ \mathbf{\Gamma}^T \end{bmatrix} \mathbf{S}^B(n+1) \begin{bmatrix} \mathbf{\Phi} & \mathbf{\Gamma} \end{bmatrix} \tag{6.13}$$

Solving the second equation of Eq. 6.12 for $f(n)$

$$f(n) = -\mathbf{W}_{ff}^{-1}\left[\mathbf{W}_{zf}^T\mathbf{z}(n) - \mathbf{\Gamma}\boldsymbol{\lambda}^B(n+1)\right] \tag{6.14}$$

and substituting the result into the first equation, results in

$$\boldsymbol{\lambda}(n) = \left[\mathbf{C}^T\mathbf{R}\mathbf{C} + \mathbf{S}^B(n)\right]\mathbf{z}(n) - \bar{\boldsymbol{\lambda}}^B(n) - \mathbf{C}^T\mathbf{R}\boldsymbol{\nu}(n) \tag{6.15}$$

where the time downdate relations are defined

$$
\begin{aligned}
\bar{\mathbf{S}}^B(n) &= \mathbf{W}_{zz} - \mathbf{W}_{zf}\mathbf{W}_{ff}^{-1}\mathbf{W}_{zf}^T \\
\bar{\boldsymbol{\lambda}}^B(n) &= \left[\boldsymbol{\Phi}^T - \mathbf{W}_{zf}\mathbf{W}_{ff}^{-1}\boldsymbol{\Gamma}^T \right] \boldsymbol{\lambda}^B(n+1)
\end{aligned}
\tag{6.16}
$$

This time downdate process involves only the constraint equations.

Comparing Eq. 6.11 and Eq. 6.15, the following measurement downdate relation can be defined

$$
\begin{aligned}
\mathbf{S}^B(n) &= \bar{\mathbf{S}}^B(n) + \mathbf{C}^T\mathbf{R}\mathbf{C} \\
\boldsymbol{\lambda}^B(n) &= \bar{\boldsymbol{\lambda}}^B(n) + \mathbf{C}^T\mathbf{R}\boldsymbol{\nu}(n)
\end{aligned}
\tag{6.17}
$$

This step refines the results of the time downdate procedure with measurement data.

A new solution method is presented in this research to save computation time and memory requirements associated with the large rank one matrix, $\mathbf{W}_{zz}$. Bryson's method is included in Appendix B. The time downdates and measurement downdates for $\bar{\mathbf{S}}^B$ and $\mathbf{S}^B$ are combined to form the equations

$$
\begin{aligned}
\mathbf{C}^B(n) &= \mathbf{C}^B(n)\boldsymbol{\Phi} \\
\mathbf{S}_{zf}^B(n) &= \boldsymbol{\Phi}^T\mathbf{C}^{B^T}\mathbf{R}\mathbf{C}^B\boldsymbol{\Gamma} + \mathbf{S}_{zf}^B(n+1) \\
\mathbf{S}_{ff}^B(n) &= \boldsymbol{\Gamma}^T\mathbf{C}^{B^T}\mathbf{R}\mathbf{C}^B\boldsymbol{\Gamma} + \mathbf{Q} + \mathbf{S}_{ff}^B(n+1)
\end{aligned}
\tag{6.18}
$$

The backward sweep starts with the final condition and the last recorded data point, $\mathbf{s}_{exp}(NT)$.

$$
\begin{aligned}
\mathbf{C}^B(NT) &= \mathbf{C} \\
\boldsymbol{\lambda}_B(NT) &= \mathbf{C}^{B^T}(n)\mathbf{R}\mathbf{s}_{exp}(NT) \\
\mathbf{W}_{zf}(1) &= \boldsymbol{\Phi}^T\mathbf{C}^{B^T}(n)\mathbf{R}\mathbf{C}^B(n)\boldsymbol{\Gamma} \\
\mathbf{W}_{ff}(1) &= \boldsymbol{\Gamma}^T\mathbf{C}^{B^T}(n)\mathbf{R}\mathbf{C}^B(n)\boldsymbol{\Gamma}
\end{aligned}
\tag{6.19}
$$

The sweep proceeds as follows, for $n = (NT - 1)$, ..., 1

$$\mathbf{K}_B(n) = \mathbf{W}_{ff}^{-1}(NT-n)\mathbf{W}_{zf}^T(NT-n)$$

$$f_B(n) = \mathbf{W}_{ff}^{-1}(NT-n)\mathbf{\Gamma}^T\lambda^B(n+1)$$

$$\bar{\lambda}^B(n) = \mathbf{\Phi}^T\lambda^B(n+1) - \mathbf{W}_{zf}(NT-n)f_B(n)$$

$$\lambda^B(n) = \bar{\lambda}^B(n) + \mathbf{C}^T\mathbf{R}\mathbf{s}_{exp}(n) \tag{6.20}$$

$$\mathbf{C}^B(n) = \mathbf{C}^B(n)\mathbf{\Phi}$$

$$\mathbf{S}_{zf}^B = \mathbf{\Phi}^T\mathbf{C}^{B^T}\mathbf{R}\mathbf{C}^B\mathbf{\Gamma} + \mathbf{S}_{zf}^B(n+1)$$

$$\mathbf{S}_{ff}^B = \mathbf{\Gamma}^T\mathbf{C}^{B^T}\mathbf{R}\mathbf{C}^B\mathbf{\Gamma} + \mathbf{S}_{ff}^B(n+1)$$

Where $\mathbf{K}_B(n)$ and $f_B(n)$ are stored for use in the forward sweep.

The matrices $\mathbf{W}_{zf}$ and $\mathbf{W}_{ff}$ require a new updating procedure in the backward sweep. $\mathbf{W}_{zz}(n)$ is not used. $\mathbf{W}_{zf}(n)$ and $\mathbf{W}_{ff}(n)$ are a function of all the previous vectors. For $i = 1, \ldots, (NT-n)$

$$\mathbf{W}_{zf}(NT-n+1) = \mathbf{W}_{zf}(NT-n+1) - \mathbf{\Phi}^T\mathbf{W}_{zf}(i)\mathbf{W}_{ff}^{-1}(i)\mathbf{W}_{zf}^T(i)\mathbf{\Gamma}$$

$$\mathbf{W}_{ff}(NT-n+1) = \mathbf{W}_{ff}(NT-n+1) - \mathbf{\Gamma}^T\mathbf{W}_{zf}(i)\mathbf{W}_{ff}^{-1}(i)\mathbf{W}_{zf}^T(i)\mathbf{\Gamma} \tag{6.21}$$

The $\mathbf{S}^B$ matrices are added.

$$\mathbf{W}_{zf}(NT-n+1) = \mathbf{W}_{zf}(NT-n+1) + \mathbf{S}_{zf}^B(n)$$

$$\mathbf{W}_{ff}(NT-n+1) = \mathbf{W}_{ff}(NT-n+1) + \mathbf{S}_{ff}^B(n) \tag{6.22}$$

All of the $\mathbf{W}$ must be updated for the next step in the backward sweep. For $i = 0, \ldots, (NT-n-1)$

$$\mathbf{W}_{zf}(i) = \mathbf{\Phi}\mathbf{W}_{zf}(i) \tag{6.23}$$

The forward sequence is unchanged from Bryson's method.

For $n = 1, \ldots, (NT - 1)$

$$
\begin{aligned}
f(n) &= f^B(n) - \mathbf{K}^B(n)\mathbf{z}(n) \\
\mathbf{s}(n) &= \mathbf{C}\mathbf{z}(n) \\
\mathbf{z}(n+1) &= \mathbf{\Phi}\mathbf{z}(n) + \mathbf{\Gamma}f(n)
\end{aligned}
\tag{6.24}
$$

f is the reconstructed force history.

Once the smoothing problem is solved, the first two coefficients of Eq. 6.5 vanish, but the third remains

$$
\delta \bar{J} = \frac{\partial \bar{J}}{\partial \mathbf{x}} \delta \mathbf{x} \equiv \bar{\mathbf{J}}_x \delta \mathbf{x}
\tag{6.25}
$$

The third coefficient is

$$
\frac{\partial \bar{J}}{\partial \mathbf{x}} = \sum_{n=0}^{N-1} \boldsymbol{\lambda}^T(n+1)\frac{\partial \mathbf{\Gamma}}{\partial \mathbf{x}} f(n) - \sum_{n=0}^{N-1} \boldsymbol{\nu}^T \mathbf{R}\frac{\partial \mathbf{C}}{\partial \mathbf{x}}\mathbf{z}(n)
\tag{6.26}
$$

This term also must vanish at a stationary point of $\bar{J}$. This is done in the outer loop where the gradient information, $\bar{\mathbf{J}}_x$, is used to improve the estimate of the impact location until a stationary point is reached. The details of the outer loop that solves this non-linear location identification problem is discussed in Section 6.3.

Since $\boldsymbol{\lambda}$, $\boldsymbol{\nu}$, f and $\mathbf{z}$ are all calculated for the other two coefficients, this third coefficient can be readily obtained. This is one of the great benefits of this smoother/filter; it provides the information necessary to update the estimate of the location.

6.2   Advantages of New Filter

The new backward sweep method offers significant computational savings for systems with a large number of degrees of freedom. The savings in required memory is described below. Similar savings are seen with the multiplication requirements.

The element of Bryson's backward filter that consumes most of the memory storage is the $\mathbf{W}_{zz}$ matrix.

In the present application there is a single force and N_{dof} degrees of freedom. Where $N_{dof} = M \times N$ (the number of x and y frequency components). The $\mathbf{W}_{zz}$ matrix then has $[N_{dof} \times N_{dof}]$ elements.

In the new formulation the large rank-one matrix is replaced with a series of vectors. The element of the filter that uses the most memory storage is the matrix multiplication in $\mathbf{S}_{zf}^{B}$

$$\mathbf{\Phi}^{T}\mathbf{W}_{zf}(i)\mathbf{W}_{ff}^{-1}(i)\mathbf{W}_{zf}^{T}(i)\mathbf{\Gamma} \tag{6.27}$$

The size of the block diagonal matrix $\mathbf{\Phi}$ is $[N_{dof} \times N_{dof}]$ and $\mathbf{\Gamma}$ is $[N_{dof} \times 1]$. The multiplication results in a $\mathbf{S}_{zf}^{B}$ matrix of size $[N_{dof} \times 1]$. One of these vectors is needed for each time step. The storage requirements are for $[N_{dof} \times NT]$ matrix.

In summary, the largest contributer to memory requirements for the new method is proportional to $N_{dof} \times NT$, as compared to N_{dof}^{2} for Bach's method.

In a problem with many degrees of freedom, as in the impact on a composite plate, the new method offers significant computational savings. The exact memory and computational time requirements of the new method and Bryson's method are compared in Table 1. With the computational savings, it is possible to attain near real-time application of the identification system to the composite plate.

6.3   The Outer Loop - The Estimate of the Impact Location

The outer loop of the inverse problem solver is the search for the impact location. The search finds the minimum of the figure-of-merit with as few calculations as possible of the filter/smoother.

The estimate of the impact location is updated using the gradient of the figure of merit J calculated in the smoother/filter. To differentiate between the local and global minima of this nonlinear problem, the search starts from multiple initial guesses and continues with a series of line searches. Among the minima found, the one with the lowest value of the figure-of-merit is taken as the global minimum.

The initial guesses are distributed throughout the area that is being monitored for

an impact. From each of these guesses a line search will start using the quasi-Newton procedure

$$\mathbf{x}_e(i+1) = \mathbf{x}_e(i) - \alpha \bar{\mathbf{J}}_{xx}^{-1}(i)\bar{\mathbf{J}}_x(i) \qquad (6.28)$$

where $\mathbf{x}_e$ is the estimate of the impact location, $\bar{\mathbf{J}}_{xx}(i)$ is the Hessian matrix, and α is the step size scaling variable. i is the counter for each line search.

The first line search starts in the direction of steepest descent, $\bar{\mathbf{J}}_{xx}(i)^{-1} = \mathbf{I}$. From the minimum of this line search another line search starts. The Hessian matrix is estimated numerically from successive values of the gradient vector $\bar{\mathbf{J}}_x$ using a rank-two update procedure. See Appendix C. The step size is determined by α. The series of searches continues until a minimum of the figure of merit is reached, when $\bar{\mathbf{J}}_x = 0$.

Within the line search, multiple evaluations of the smoother/filter are performed to find the minimum of the figure-of-merit along the line. The line search starts by taking the maximum step size in the direction determined from Eq. 6.28. The next step will be along the line but half the size of the first, either forward or backward. The direction is determined by

$$\kappa = \frac{\bar{\mathbf{J}}_x(0) \cdot \bar{\mathbf{J}}_x(j)}{\left|\bar{\mathbf{J}}_x\right|} \qquad (6.29)$$

where

$$
\begin{aligned}
\bar{\mathbf{J}}_x(j) &= \quad \text{gradient at current point of line search} \\
\bar{\mathbf{J}}_x(0) &= \quad \text{gradient at initial point of line search} \qquad (6.30) \\
\left|\bar{\mathbf{J}}_x\right| &= \quad \text{the magnitude of the vector}
\end{aligned}
$$

and j is the counter within the line search.

If $\kappa > 0$, then the search has not reached the minimum, and the search continues forward. If $\kappa < 0$, then the minimum has been passed, the gradient has changed sign, and the search takes a step back. The minimum of the line search will then be reached after several evaluations of the smoother/filter, see Figure 13.

The maximum error, ϵ_{ls}, and range, L, of the line search can be calculated from

$$\epsilon_{ls} = \frac{l}{2n_{ls}}$$

$$\tag{6.31}$$

$$L = l\left(1 + \frac{2^{n_{ls}-1} - 1}{2^{n_{ls}-1}}\right)$$

where

$$l = \text{maximum step size of line search}$$
$$\tag{6.32}$$
$$n_{ls} = \text{number of smoother/filter evaluations per line search}$$

The objective of the search technique is to minimize the number of times the smoother/filter is used to update the estimated location while searching for the global minimum in the figure of merit. Several tests were used to control the start and continuation of each line search. The following tests were designed to avoid searching in an area far from the impact and to finish the search close to a minimum. Because experimental data is used, it is not practical to look for an exact zero in the gradients of the figure-of-merit contour. If the gradients are less than a preset tolerance, they are considered zero.

- If the gradient of the figure-of-merit, $\bar{\mathbf{J}}_x$, is near zero at the initial point of a line search, the search is cancelled. Either the estimated location is very far from the impact or is already at a minimum. The value of J is stored as a possible global minimum.

- If the value of J at the end of the line search has not decreased by 10% or more from the starting point of the search, then the search is cancelled. This is an additional safeguard against searching in flat regions of the figure of merit contour.

- If the line search is perpendicular to the direction of steepest descent, the search is cancelled. This allows for an early exit from the line search if the minimum is reached before the maximum number of evaluations.
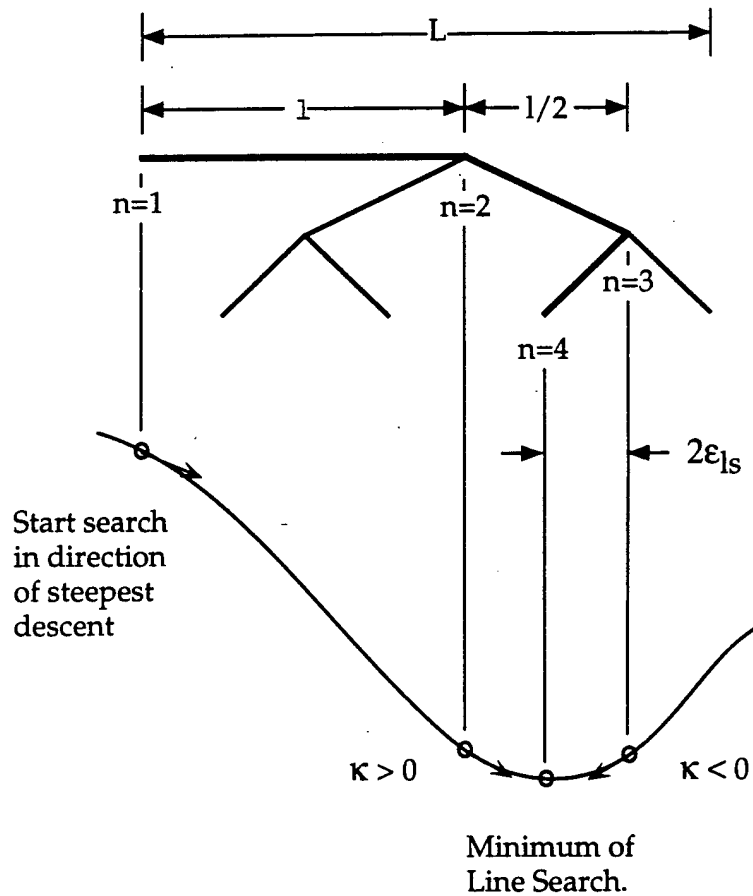
Figure 13: The line search. The line search continues through a series of branch points. The gradient of the figure-of-merit is used to guide the search. The search is ended when the gradiant of J is less then the preset tolerance.

Table 1: The computational advantages of the new backward filter for systems with a large number of degrees of freedom. N_{dof} is the number of degrees of freedom in the system and NT is the number of time steps.

	Present Method	Previous Method
Number of multiplies	$8 \times N_{dof} \times NT^2$	$3 \times N_{dof}^2 \times NT$
Elements to store	$10 \times N_{dof} \times NT$	$3 \times N_{dof}^2$

Chapter 7

Computer Code - IDIMPACT

With the theory of the identification system developed in the previous chapters, the system was implemented with the computer code IDIMPACT. As indicated in Figure 14, IDIMPACT uses the digitized plate reponse and application specific parameters to identify the impact and report the results in a graphic interface. The code provides near real-time impact identification.

The next chapter presents the application of IDIMPACT to a composite plate.

Identification system
computer code

| Graphic Interface |

Plate
response → IDIMPACT → Location

Application
parameters →

F

time
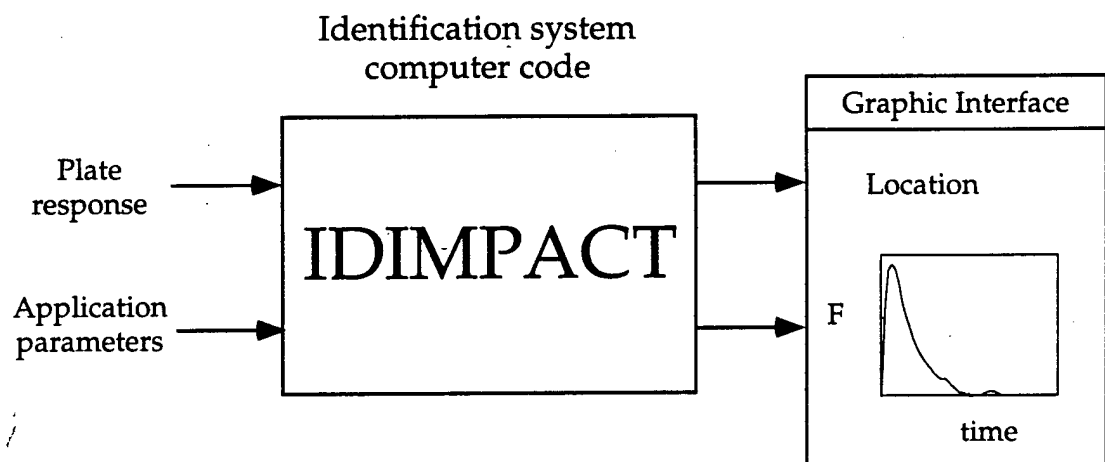
Figure 14: The input and output of IDIMPACT.

Chapter 8

Application of IDIMPACT

With the theoretical development and computer implementation of the identification system, the next step is designing the system for a specific application. Application parameters are specified for each component of the identification system. The system was applied to the $T800$ composite plate described in the Chapter 5.

The objective in designing the system is to keep the total solution time of the force identification to a minimum. The solution time is consumed mostly by the smoother/filter in the inverse problem solver. To keep the solution time down, the solution time of the smoother/filter and the number of times the filter is called must be kept to a minimum. The speed of the smoother depends on the forward model. The number of times the smoother is called depends on the outer loop of the inverse problem solver - the search for the impact location.

An example impact was used to demonstrate all of the components of the identification system.

8.1 Experimental Setup

The experimental setup includes the composite plate, sensor array, instrumented hammer, data acquisition system and computer controller and processor. The system was designed so that the data could be acquired and processed using one computer.

The following hardware and software items were used:

- $T800[45/90/-45/0/0/45/0/0/-45/0]_s$ carbon composite plate described in Chapter 5. In this application the plate had free boundaries with support only in the corners. The example impact was at $(x, y) = (12.5, 5.0)$.

- Piezo Kinetics Incorporated, PKI-400 .25 inch diameter disk, piezoelectric sensors discussed in Chapter 4. The response of the plate to the impact was measured using a thirteen sensor array of piezoelectrics bonded to the composite plate. An area of 20 inches by 20 inches was covered. The geometry is shown in Figure 15. Each sensor was grounded to the composite plate.

- PCB Piezotronics instrumented hammer, 208 A04 force transducer and 480A power unit. The output of the load cell was recorded for comparison to the reconstructed force.

- National Semiconductor LF 412 operational amplifier. The amplifiers were used for the sensors and the instrumented hammer.

- Kiethley Metrabyte DAS 1800 analog to digital signal converters. Each board has eight channels with a maximum conversion rate of 333Msamples/sec.

- NCA 133MHz pentium computer.

- Keithley Metrabyte VTX controller for the DAS1800.

- Microsoft Windows 95.

- Microsoft C++ and Visual Basic.

The data acquisition system was controlled by the VTX controller operating in Visual Basic. It was triggered by the voltage output of the instrumented hammer. When the signal from the hammer crosses a predetermined threshold, a TTL trigger signal is sent to the data acquisitions boards. The voltage was amplified to reduce noise and to provide a zero offset. The hammer amplifier is described in Figure 17.

Once the data acquisition is triggered the voltage generated by the sensors is digitized at 22.3 KSamples/sec. 150 data points from each channel are recorded - 10

pre-trigger and 140 post trigger. The piezoelectric sensors are very sensitive to strain and unamplified easily produce output over ten volts. Amplifiers provided a zero offset for the sensor voltage output. The sensor amplifier is described in Figure 16.

Once the data is digitized, processing can begin. IDIMPACT, described in Chapter 7, operates in the 32 bit environment of Windows 95.

8.2   Sensor and Preprocessor

The gain of the sensors was determined by comparing the response of the forward model with the measured response. $g_\epsilon = 4.0 \times 10^{-6}(1/volts)$.

The preprocessor divided the full 20 inch by 20 inch sensor array into five overlapping regions each with five sensors. (Five sensors were used $NS = 5$.) After scanning the sensors to determine which had the highest initial energy, one of the regions is chosen to be used by the inverse problem solver. The geometry of the isolation regions, the definition of the global and local coordinate systems, and the sensor numbering system are shown in Figure 18.

With the example impact at $(x,y) = (12.5, 5.0)$, the region of five sensors with the highest initial energy was the the lower-right region, region four. The sensor readings at these five sensors is shown in Figure 19. In the local coordinates of isolation region four, the impact is at $(x', y') = (2.5, 5.0)$

The different energy content in the initial time window of the sensors at different distances from the example impact is shown in Figure 20. With the example impact, sensor 4 located at $(x, y) = (10, 0)$ is 5.59 inches from the impact while sensor 5 located at $(x, y) = (20, 0)$ is 13.5 inches from the impact. The time window, selected so the sensor farther away would have a very small energy content compared to the close sensor, was 26.9×10^{-5} seconds. This corresponds to the first seven data points in the sensor data. $N_e = 7$.
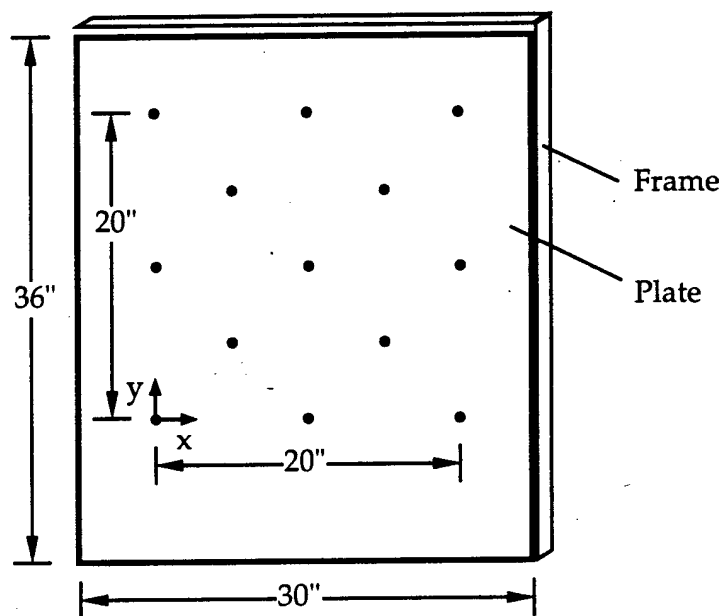
Figure 15: The composite plate with the dimensions and geometry of the thirteen piezoelectric sensor array. The global coordinate system is shown. The sensors are on the back of the plate. The plate with free boundary conditions is shown.
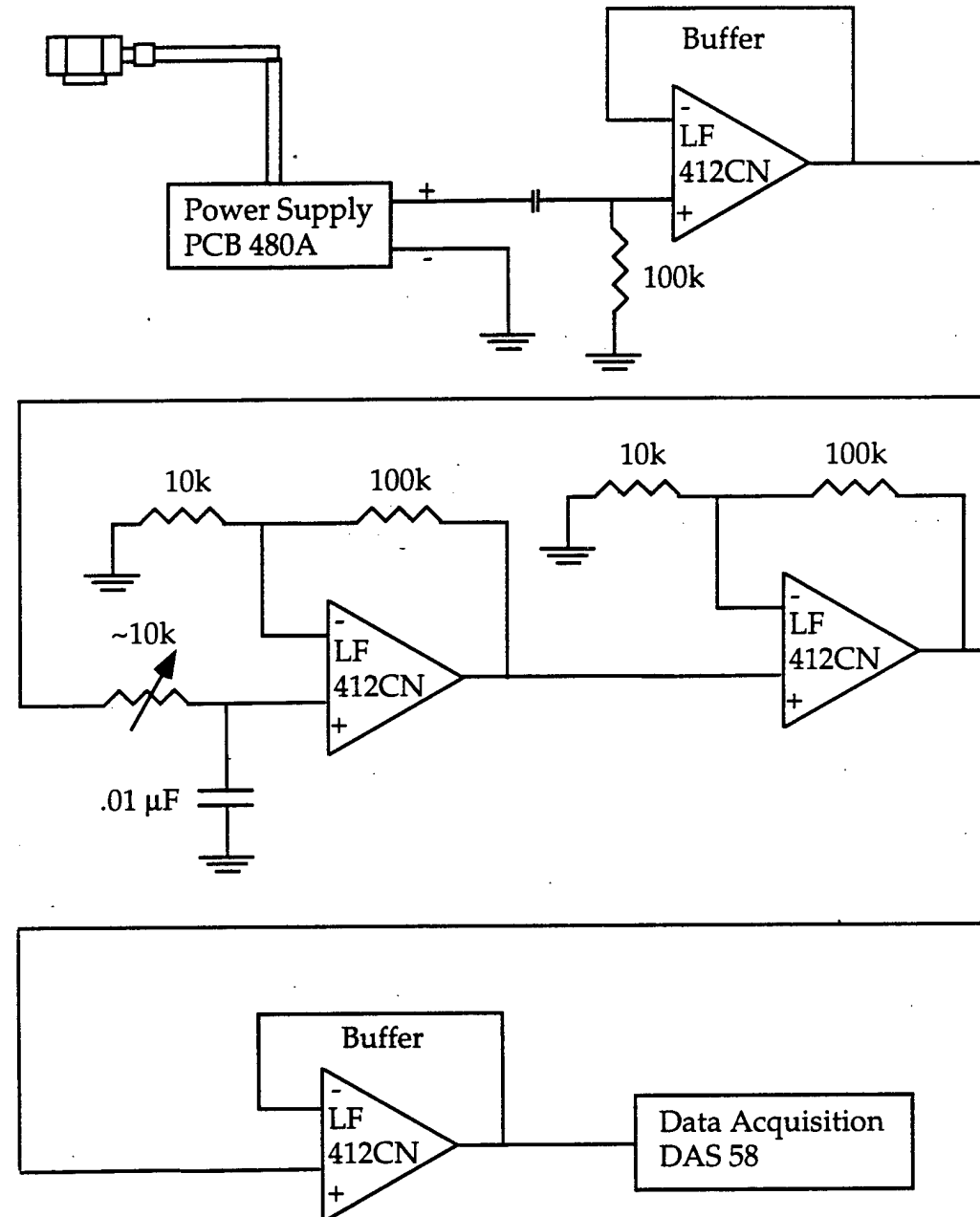
Figure 16: Wire diagram of hammer amplifier.

Amplifier

Sensor

LF
412CN

Data Acquisition
DAS 58
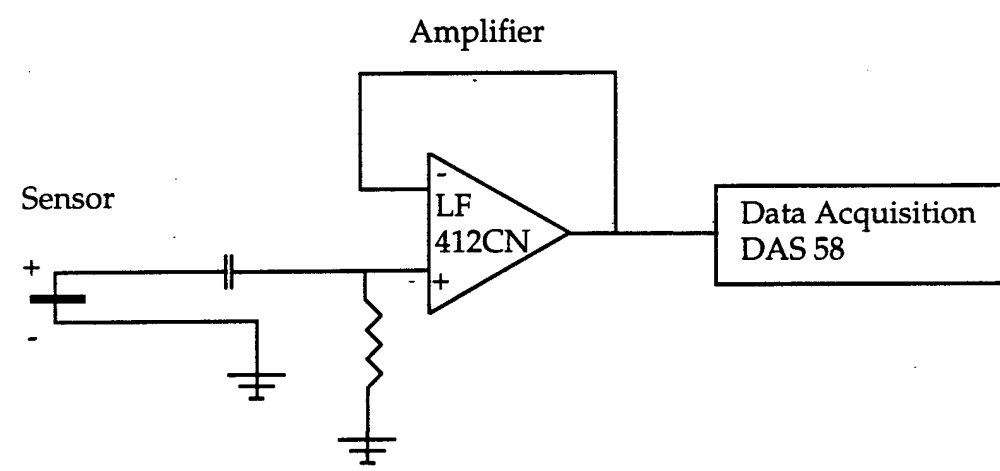
Figure 17: Wire diagram of sensor amplifier. No amplification is applied but
the operational amplifier is used to provide a zero offset to the
signal.
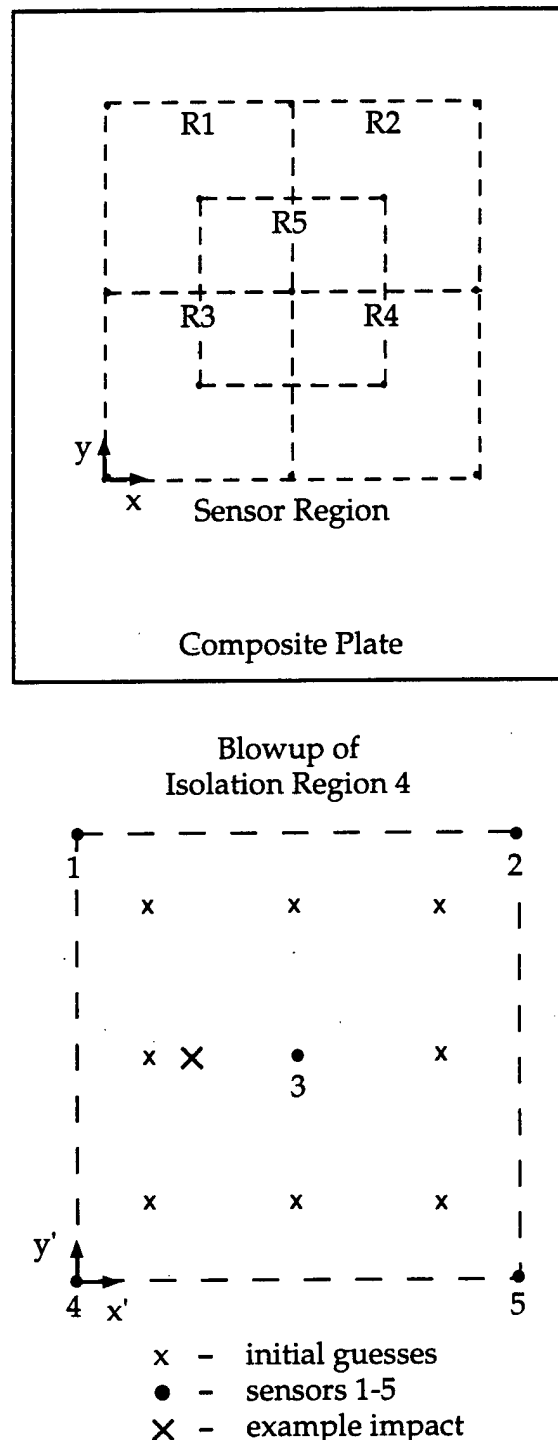
Figure 18: The sensor array and the five overlapping isolation regions, R1-R5. The global coordinates (x, y) and the local isolation region coordinates (x', y') are shown.
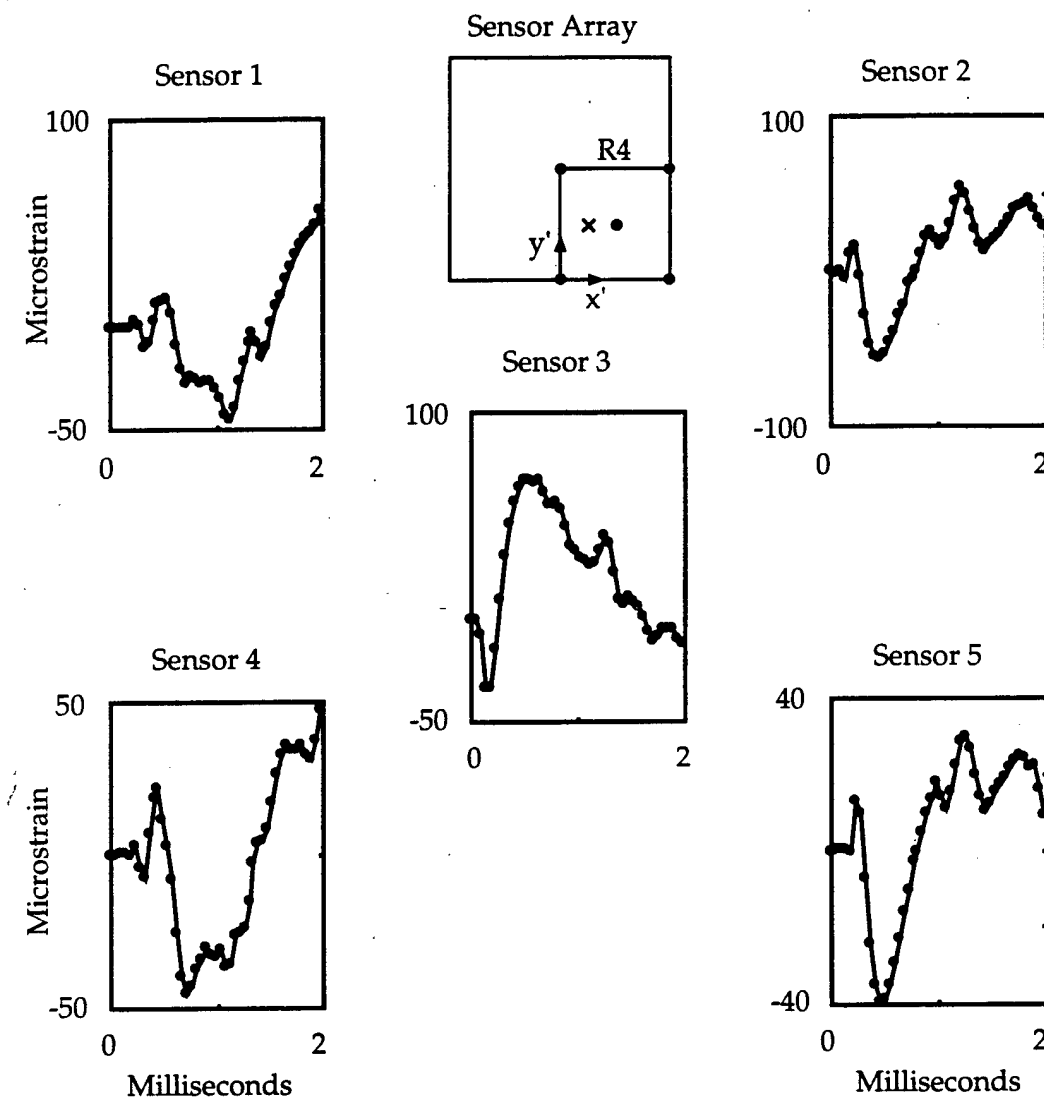
Figure 19: The response of the five sensors in isolation region four. The impact was reported at $(x', y') = (2.7, 5.2)$. The actual impact was at $(x', y') = (2.5, 5.0)$.
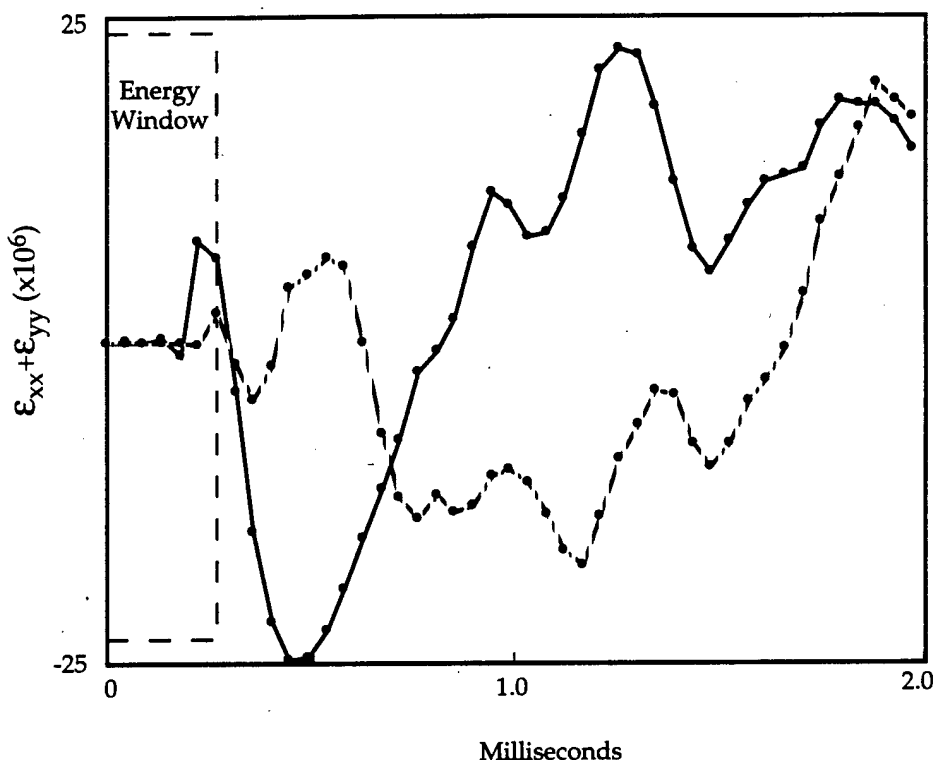
Figure 20: Response of the sensor at $(x', y') = (0.0, 0.0)$ (solid line) and at $(x', y') = (10.0, 0.0)$ (dashed line) to the example impact. The energy window is used to determine the sensors closest to the impact.

8.3   Forward Model

The forward model must accurately estimate the plate response while using as few time steps and frequency components as possible. The time steps and frequency components determine the solution time of the inverse problem solver.

The periodic solution of the Fourier transform can lead to an error, aliasing, when the solution overlaps. It is necessary to have a large spatial domain to prevent overlapping as the wave propagates. The spatial domain was set to $X = Y = 90$ inches. To maintain the spatial resolution, many frequency components were needed, $M = N = 180$.

The time duration of the measured data has to be long enough to include the full impact force history. The duration of the impact was approximately one millisecond. Two milliseconds of data was recorded to insure all of the force was included. The number of time steps, NT, was 45, the time step, Ts, was 4.48×10^{-6} seconds. This results in a total time duration of $Ts \times (NT - 1) = 1.97$ milliseconds.

For this application, it was discovered that the frequency components beyond the first 36 were essentially zero. Instead of using all the components in the solution, the 144 near zero components were treated as zero padding. A great deal of computation time is saved using only the non-zero components.

8.4   Inverse Problem Solver

The outer loop of the inverse problem solver, the search for the impact location, must be designed so that the impact is located with as few evaluations of the inner loop, the smoother/filter, as possible while still maintaining the robustness of the system.

The weighting values for the smoother/filter were determined in Chapter 6. The values **Q** and **R** were set to .05 and 5.0×10^{10}.

To help design the search technique, an exhaustive search was performed for the example impact. The smoother/filter calculated the figure of merit, J, on a grid with 1/2 inch spacing in the isolation region. This creates a figure-of-merit contour. The

minimum of this contour is the identification system's estimate of the actual impact location. The typical contour has one global minimum and several local minima, see Figure 21.

There are three components of the search technique to be designed for this contour, the number and spacing of the initial guesses, the accuracy and range of the line search, and the tests to control the start and continuation of each line search.

There has to be enough initial guesses distributed over the search region to assure that the global minimum can be found. It was observed from experiment that with an impact near the edge of the sensor array, it was difficult to find the contour leading to the minimum of the figure-of-merit. With an impact near the middle, it was relatively easy to find the correct contour. To assure that the global minimum could be found, the initial guesses were distributed near the search region boundary. The initial guesses are shown in Figure 18.

To maintain a robust search, there should be an overlap in the range of each search. The maximum step size, l, of the first line search was chosen as 1.6 inches with 3 evaluations of the filter/smoother, $n_{ls} = 3$. The successive line searches were limited to a step size of 1.0 inches and 3 function evaluations. Using Eq. 6.31, the range for the first line search is 2.80 inches and for the successive searches is 1.5 inches. Since three successive line searches are allowed, the maximum total range of each search is 5.8 inches. The maximum error for the minimum of the first and successive line searches is .27 and .25 inches. The accuracy and overlapping searches provided good results for the application to the $T800$ composite plate.

The preset tolerance for the gradiant needed to start a search was $\bar{J}_e = 40$. The tolerance needed to approximate a minimum of the figure-of-merit was $\bar{J}_e = 15$. If $\bar{J}_e < 40$, the search was not started from the initial guess. If $\bar{J}_e < 15$, the search was stopped because a minimum was found.

The new formulation of the smoother/filter offers a great computational advantage for this application. With the number of non-zero frequency components and time steps in the forward model, there is a 91% saving in the computational time and an 88% savings in the memory requirements for the new filter, see Table 2. The computational savings were calculated using the relations in Table 1. (Eight bytes
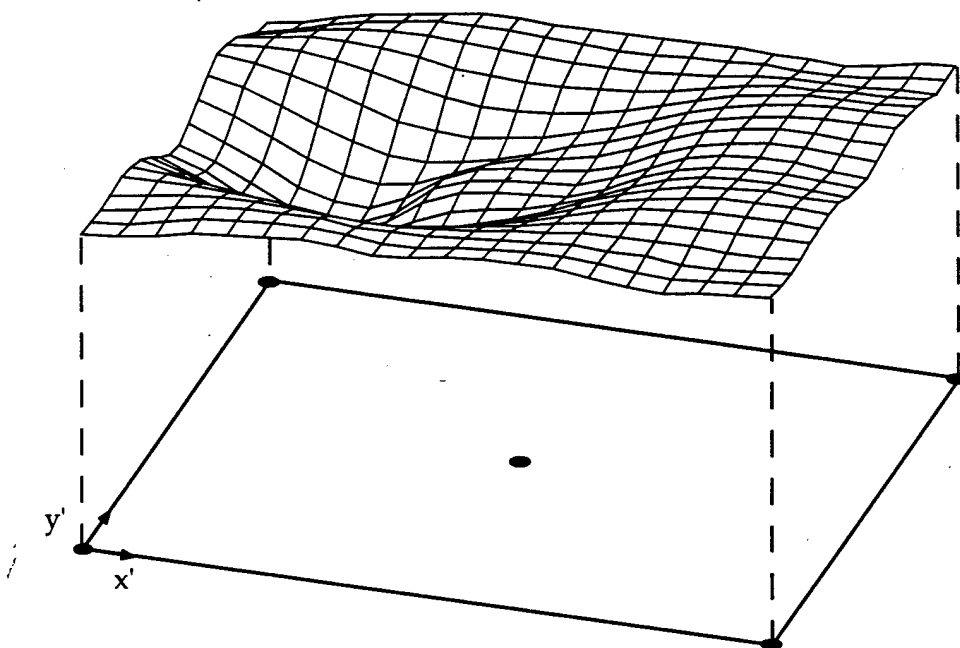
Figure 21: The figure of merit contour. The smoother/filter evaluated the figure-of-merit on a 1/2 inch grid in the isolation region. The actual impact was at $(x', y') = (2.5, 5.0)$

are stored per double on the personal computer.)

8.5   Identification of the Example Impact

With all of the application parameters determined, IDIMPACT was run to identify the example impact. From two starting points, the impact was found, see Figure 22. The two line search stopped at slightly different points because the searches are limited to three consecutive line searches. The searches starting from the upper right and lower right corner were cancelled because the value of the figure of merit at the end of the line search had decreased by less than 10% from the starting point. The searches were not started from the other initial guesses because the gradiant was below the preset tolerance, $\bar{J}_e < 40$. The impact was reported .28 inches from the actual location and the total impact energy reported was within 12% of the actual.

A total of 32 evaluations of the smoother/filter was needed to complete the search. On the PC, each function evaluation took 8 seconds for a total solution time for the identification system of 4 minutes and 16 seconds. The performance of the identification system allows near-real time application of IDIMPACT.

The reconstructed force is compared to the experimentally recorded force in Figure 23.

+ Search starting point   + Line search end point
O Best estimate of impact   ● Sensor location
     location
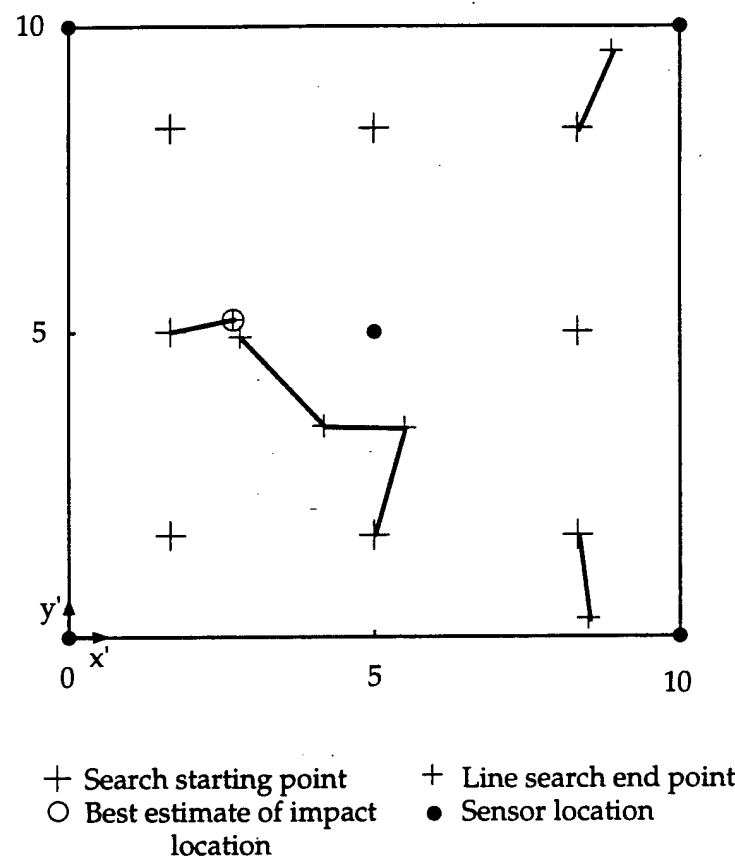
Figure 22: Search using multiple starting points. The search starting from $(x', y') = (1.6, 5.0)$ successfully found the impact location. The reported impact location was at $(x', y') = (2.7, 5.2)$ while the actual location was $(x', y') = (2.5, 5.0)$.
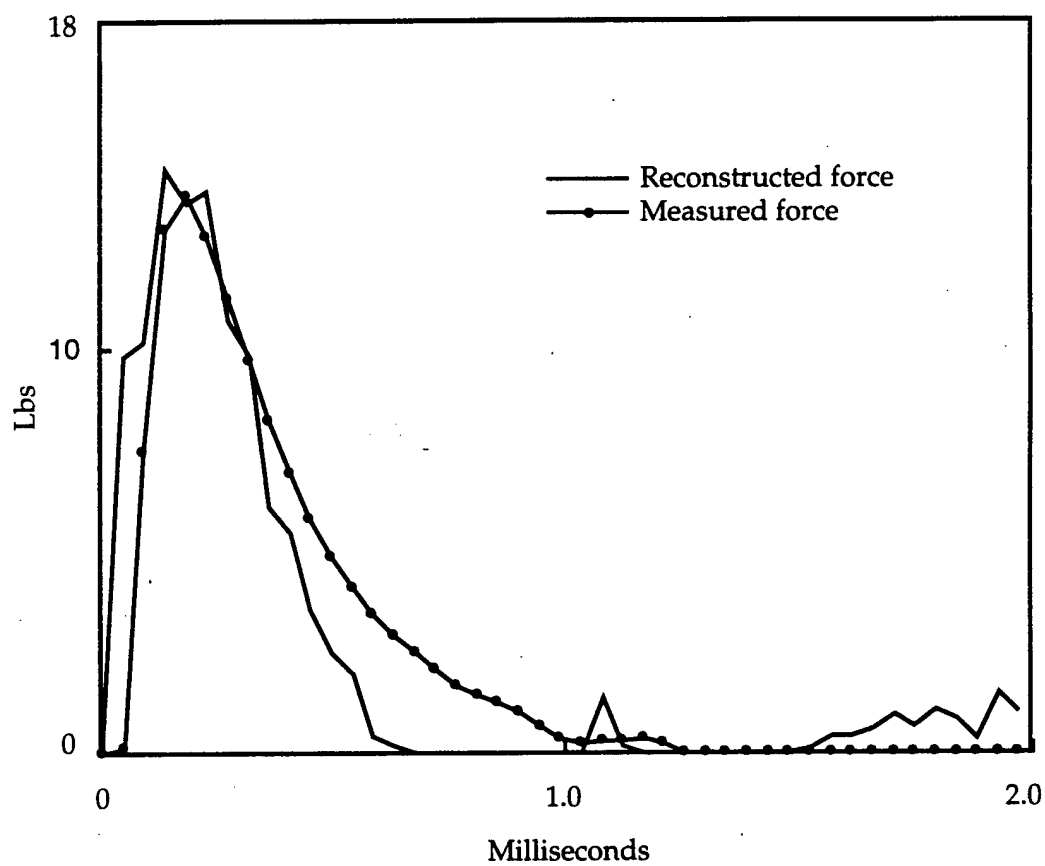
Figure 23: The reconstructed force compared to the example impact.

Table 2: The new filter applied to the plate impact identification problem. To model the plate response, 36 frequency components in the x and y direction were used with 45 time steps.

	Present Method	Previous Method	Percent Savings
Number of multiplies	21 Million	227 Million	91
Memory Required	4.7 MBytes	40.3 MBytes	88

Chapter 9

Identification System Accuracy and Robustness

In the previous chapter the identification system was designed and applied to the $T800$ composite plate. The system successfully identified the example impact. In this chapter the identification system will be tested with numerous impacts to quantify the error in its estimate of the impact location and the force reconstruction. The system will be tested on the plate with clamped and free boundary conditions. Also, to further test the robustness of the system, a noisy environment will be simulated.

9.1 The Test Impact Array

An array of impacts was applied to the composite plate. The distribution of 40 impacts is shown in Figure 24. The impacts were distributed over a quarter of the plate, isolation region 4. Because the plate is symmetric, the results from the region represent whole sensor array.

A direct hit over the sensor was not included in the impact distribution due to a limitation of the data acquisition system. With an impact very near a sensor, the sensor output will exceed 10 volts. This saturates the sensor channel on the analog to digital converter. The other sensor channels are also affected and the digitized data is not accurate. With the saturated data and the inaccurate data, it is not possible

for the identification system to identify the impact. This limitation can be overcome with improvement in the acquisition system; it is not a theoretical limitation of the identification system.

9.2   Free Plate Boundaries

The impact test array was applied to the composite plate with the free boundary conditions. The reported location results are shown in Figure 25, where the actual impact is at the center of the circle and the reported impact is in error in the x or y direction. The reported impact location was, on the average, 0.39 inches from the actual impact location. 71.1% of the impacts were within 0.5 inches of the actual.

The error in the energy of the reconstructed force is defined as

$$
\begin{aligned}
\epsilon_f &= \frac{|E_{recon} - E_{exp}|}{E_{exp}} \\
&= \frac{\left| \sum_{n=0}^{NT-1} f^2(n) + \sum_{n=0}^{NT-1} f_{exp}^2(n) \right|}{\sum_{n=0}^{NT-1} f_{exp}^2(n)}
\end{aligned}
\tag{9.1}
$$

where E_{recon} and E_{exp} are the energy of the reconstructed force and the experimentally recorded force. f_{exp} is the recorded force from the instrumented hammer. The energy of the reconstructed force differed by an average of 14.2% from the recorded impact. The average error in the peak magnitude was 3.1%. The reconstruction of the example impact was shown in the previous chapter, Figure 23.

Noise was added to the digitized data obtained from the impact test array. This simulated noise was calculated using

$$
\begin{aligned}
\mathbf{V}_{noise} &= \mathbf{V}_{exp} + 0.5 \times Randn \\
\mathbf{S}_{noise} &= g_\epsilon \times \mathbf{S}_{exp}
\end{aligned}
\tag{9.2}
$$

where the *Randn* function randomly generates a normal distribution of numbers with a mean of 0.0 and a variance of 1.0. The noise generated is approximately 10% of the magnitude of the original experimental data. The plate response to the example impact with added noise is shown in Figure 26.

The reported location results are shown in Figure 27. The average impact reported for the noisy case was .41 inches from the actual. 73.7% of the impact were located within 0.5 inches of the actual. The example impact was reported at $(x', y') = (3.0, 5.3)$.

The energy of the reconstructed force history was on the average within 11.8% of the recorded impact history. The average error in the peak magnitude was 2.0%. The reconstruction of the impact at the example location is shown in Figure 28.

9.3   Clamped Plate Boundaries

The impact array was also used to test the identification system on the plate with clamped boundaries. The reported location results are shown in Figure 30. The average error of the reported impact was .47 inches. 66.7% were found with 0.5 inches. The example impact was reported at $(x', y') = (2.7, 5.1)$.

The example impact is reconstructed in Figure 31. With the forty impacts tested, the average energy of the reconstructed force was within 13.4% percent of the experimentally recorded force. The magnitude of the force was reconstructed within 8.25%.

Noise was also added to the data recorded with the clamped boundary conditions. The results are in Figure 33. The average error of the reported impact was .49 inches. 60.5% were found with 0.5 inches. The example impact was reported at $(x', y') = (2.7, 5.1)$.

The example impact is reconstructed in Figure 31. The average energy of the reconstructed force was within 16.3% percent of the experimentally recorded force. The magnitude of the force was reconstructed within 9.5%.

Array of test impacts in region 4
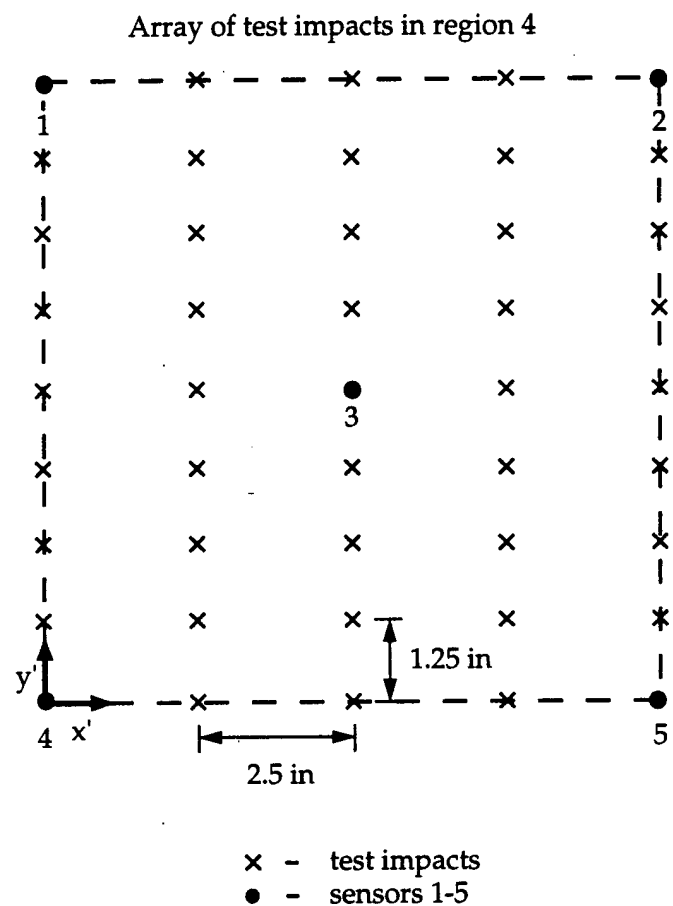
Figure 24: Array of impacts in isolation region 4 used to test the identification system.
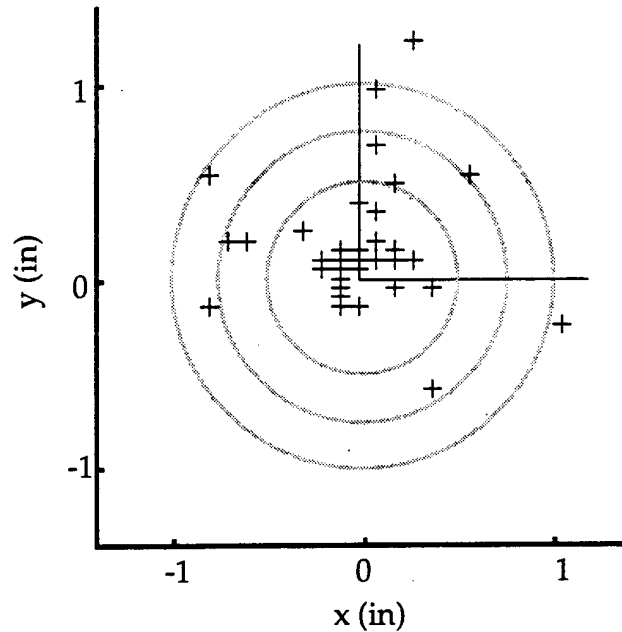
r(in)	Percent Within
.50	71.1%
.75	84.5%
1.0	92.1%

maximum error is 1.28 inches

Figure 25: Results from ten inch sensor spacing with free plate boundaries.
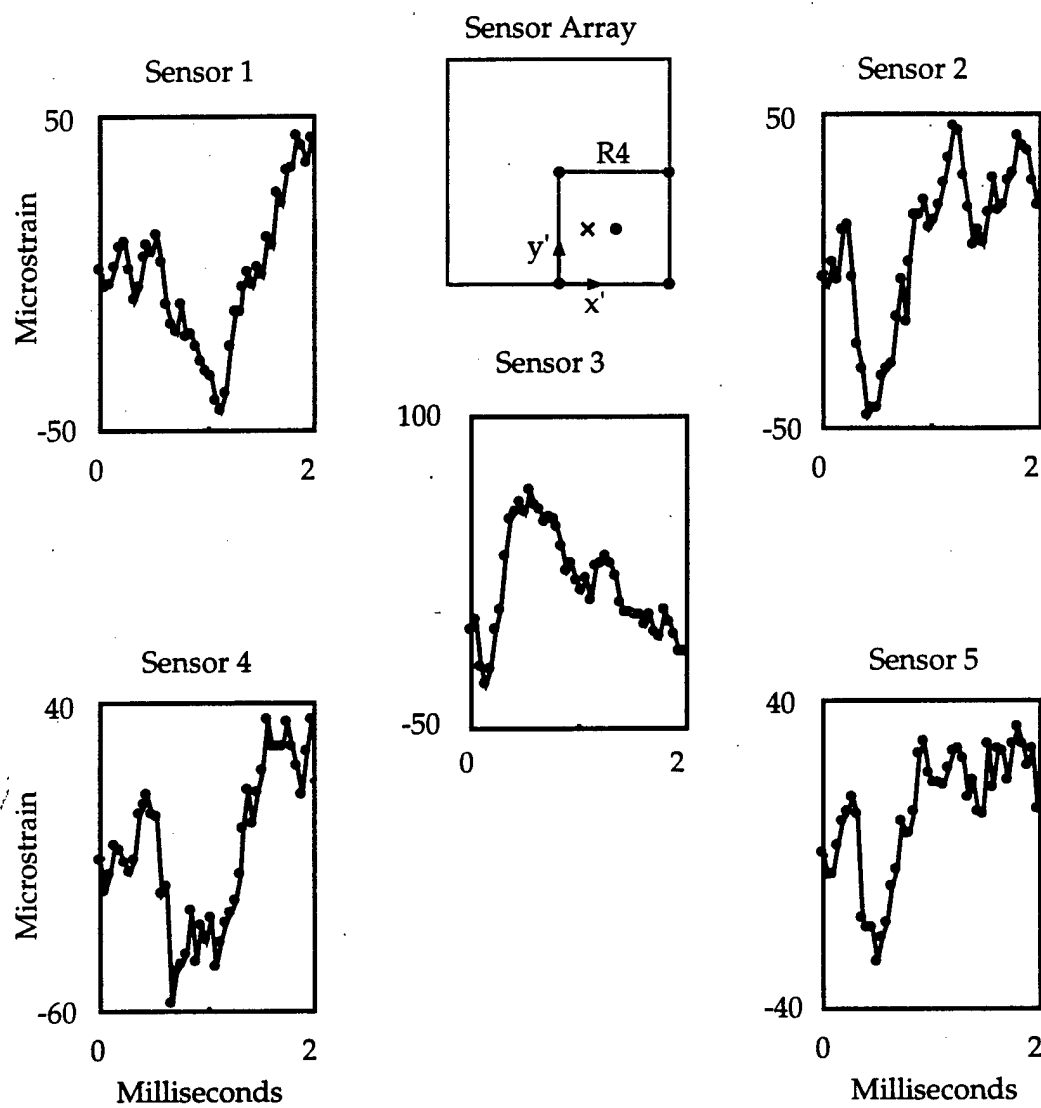
Figure 26: The response of the example impact with noise added to the sensor response. The plate has free boundary conditions.
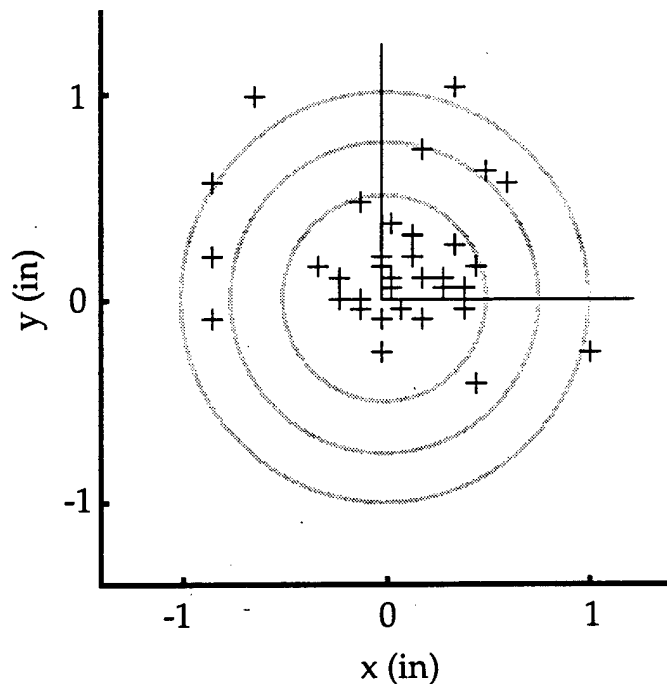
r(in)	Percent Within
.50	73.7%
.75	79.0%
1.0	92.1%

maximum error is 1.12 inches

Figure 27: The accuracy of the impact identification system with the noisy sensor measurement and the free boundary conditions.
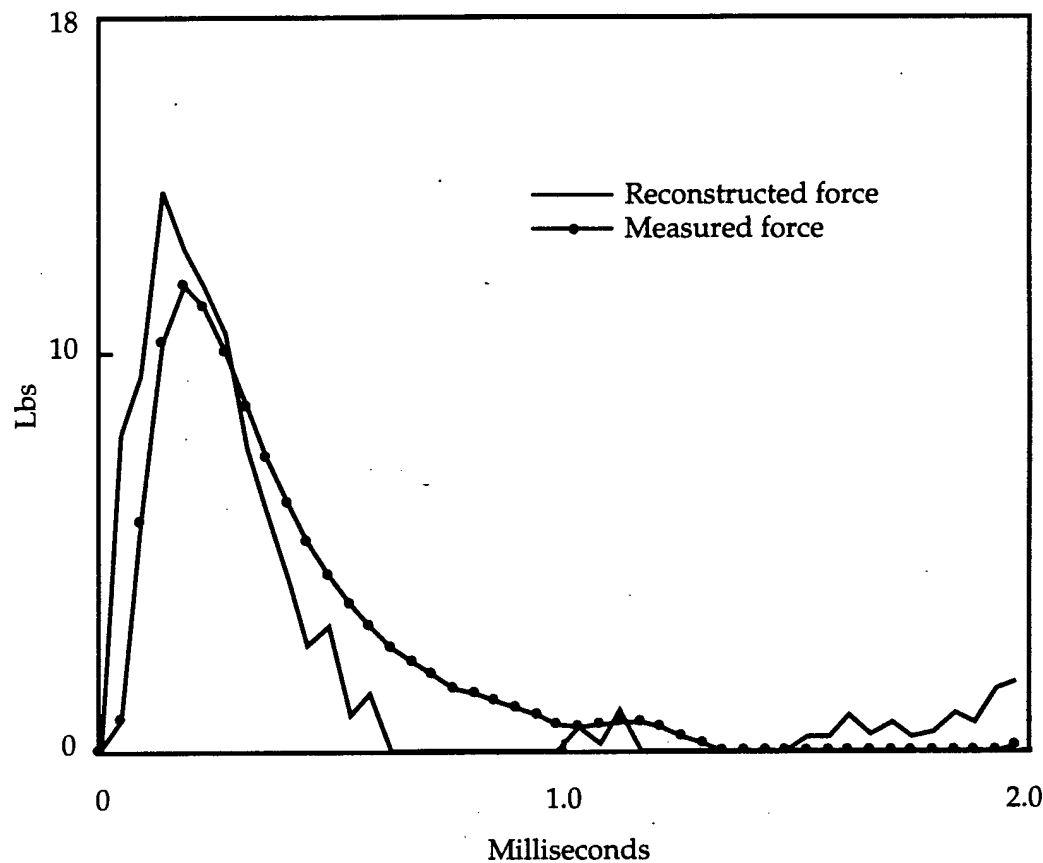
Figure 28: The reconstructed force with noise in the recorded sensor data. The example impact at $(x', y') = (2.5, 5.0)$ was reported at $(3.0, 5.3)$. The plate has free boundary conditions.
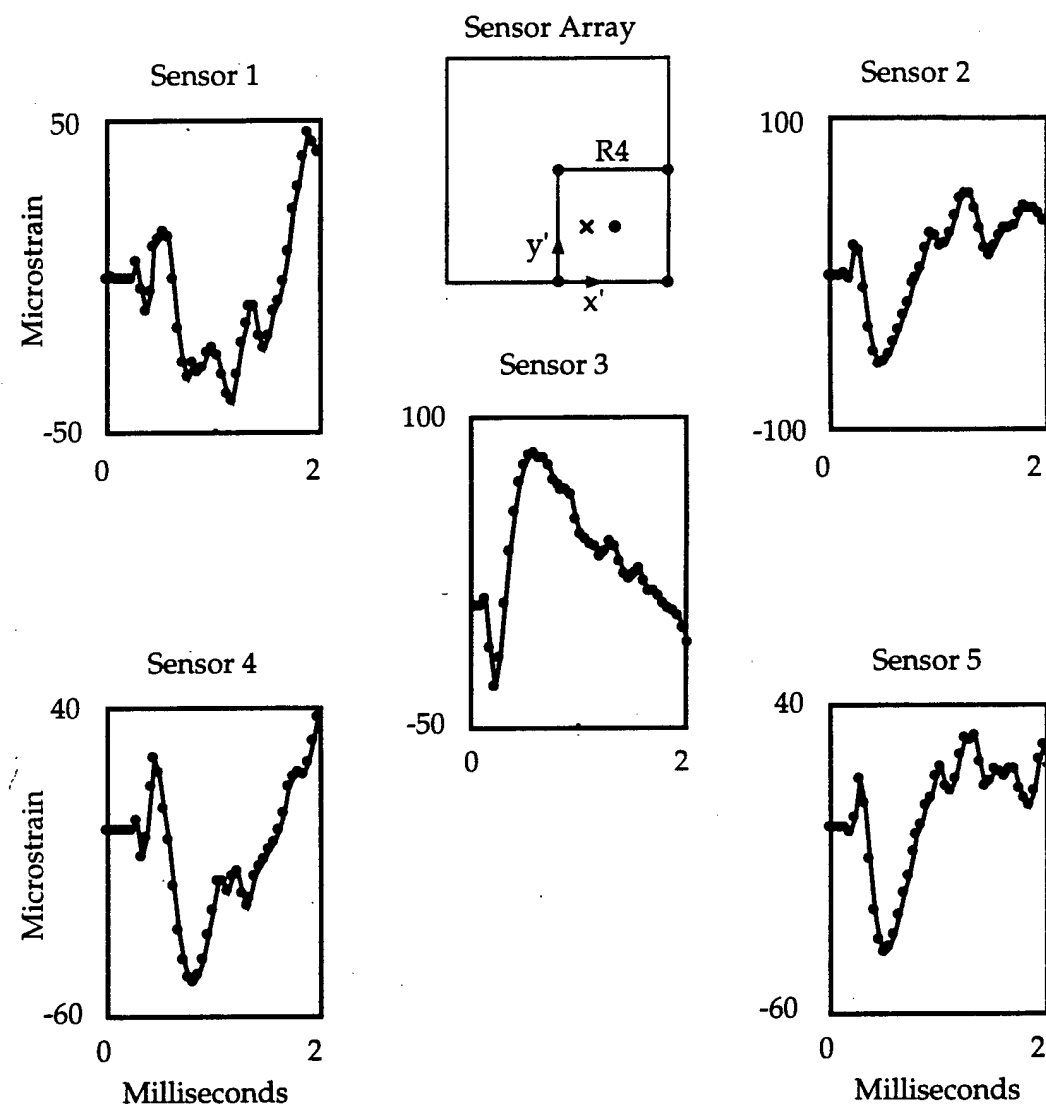
Figure 29: The response of the five sensors to an impact at $(x', y') = (2.5, 5.0)$. The boundaries of the plate are clamped.
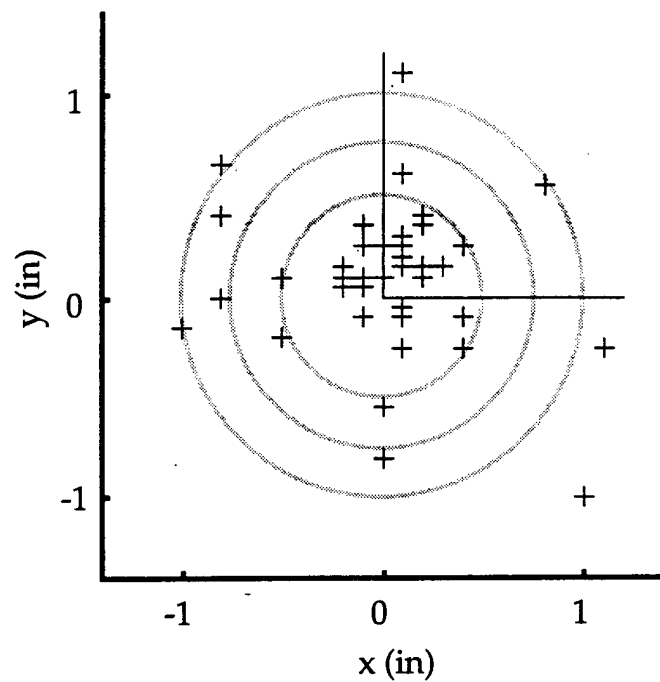
r(in)	Percent Within
.50	66.7%
.75	76.9%
1.0	87.2%

maximum error is 1.41 inches

Figure 30: Result from sensor array with clamped plate boundaries.
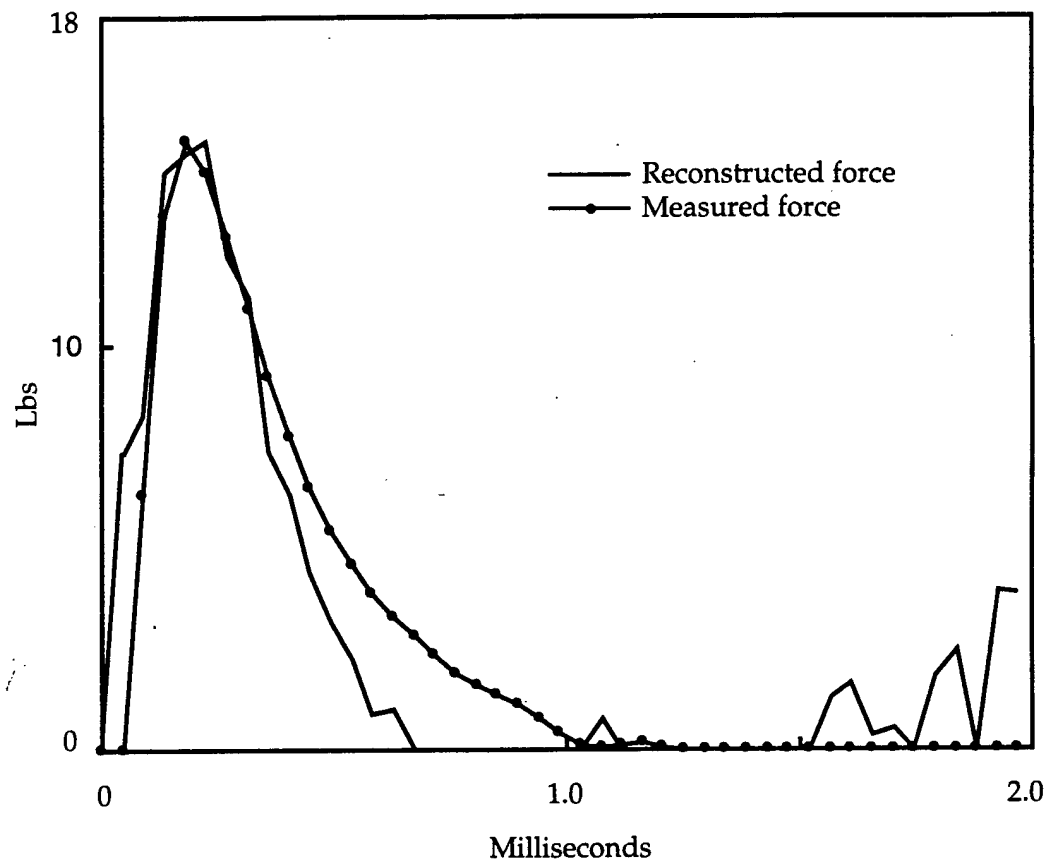
Figure 31: The typical reconstructed force history for the clamped boundary. This is the impact reconstruction for the impact at $(x', y') = (2.5, 5.0)$. The reported impact was at $(x', y') = (2.7, 5.1)$
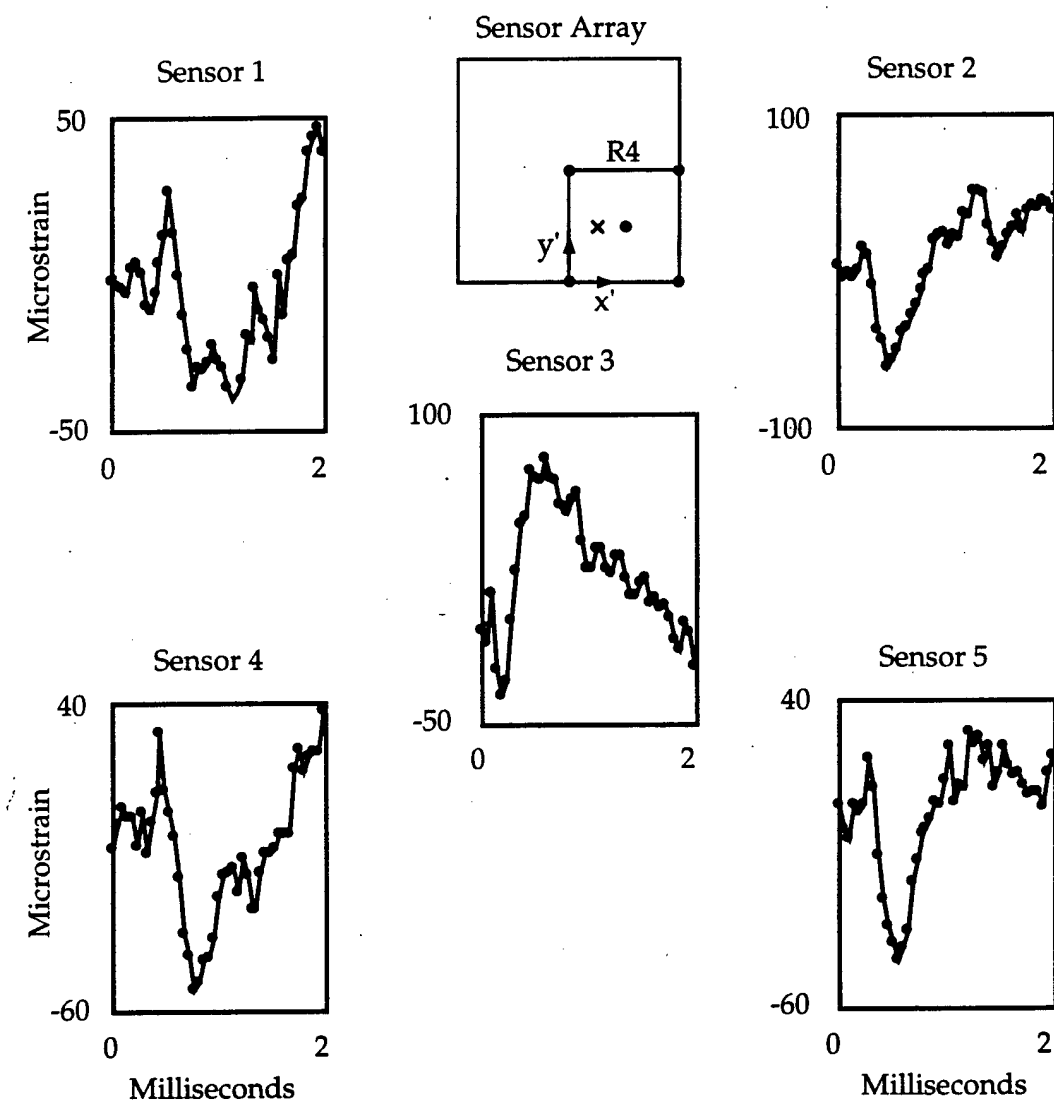
Figure 32: The response of the five sensors to an impact at $(x', y') = (2.5, 5.0)$. The boundaries of the plate are clamped and noise is added to the sensor data.
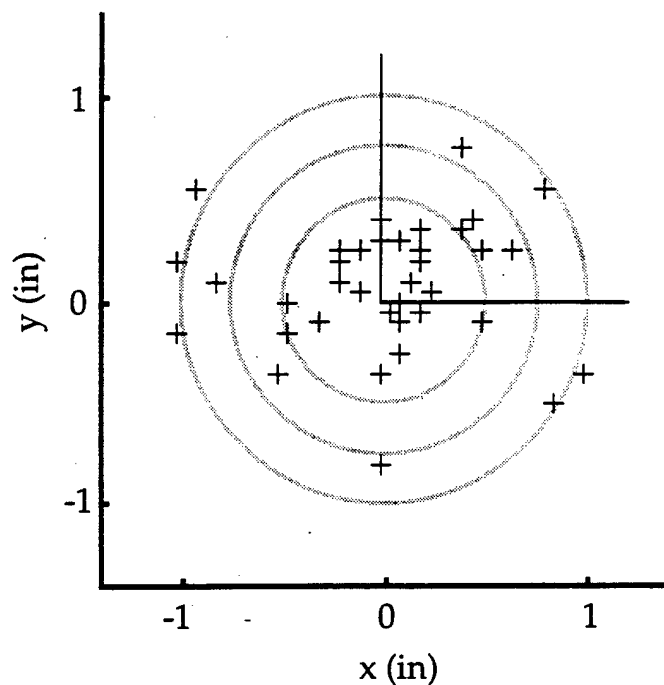
r(in)	Percent Within
.50	60.5%
.75	76.3%
1.0	89.5%

maximum error is 1.06 inches

Figure 33: Result from sensor array with clamped plate boundaries and noise added to sensor data.
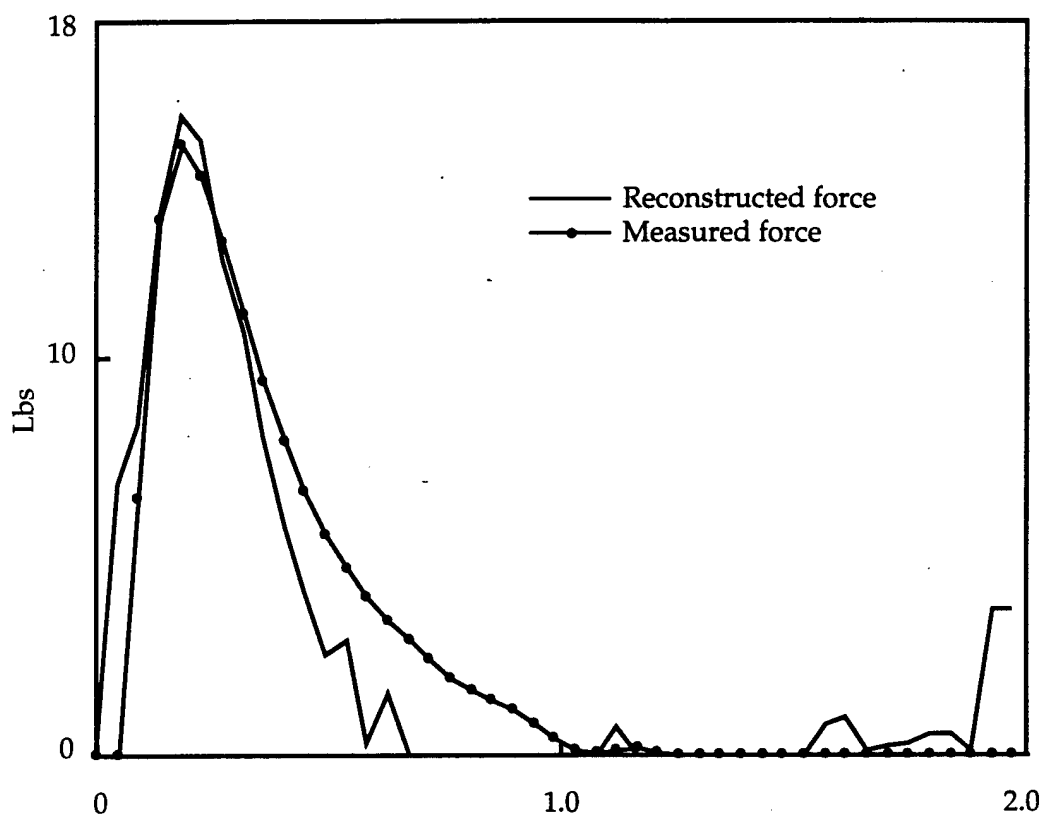
Figure 34: The typical reconstructed force history for the clamped boundary with noise added to the sensor data. This is the impact reconstruction for the impact at $(x', y') = (2.5, 5.0)$. The reported impact was at $(x', y') = (2.7, 5.1)$

9.4   Discussion of Results

The identification proved to be a very reliable and robust system for locating and reconstructing the force time history of an unknown impact. The system had very accurate and consistent performance in the four cases tested: the composite plate with free or clamped boundary conditions and with clean or noisy data. The average reported location differed by .39 inches for the free boundary case to .49 inches for the clamped plate with noise added to the sensor data. The best match between the modal response and the experimental response was achieved with the free plate boundaries.

The most significant error in the reported location occured when the impact was close to a sensor on the edge of the sensor array. For example, the largest error of the clamped boundary case was 1.06 inches. This occured when the plate was hit at $(x', y') = (10, 1.25)$. The nearby sensor, sensor 5 at $(x', y') = (10.0, 0.0)$, measures strain of significantly greater magnitude then the other sensors in the isolation region. In the search for the impact location, this sensor has a big effect on the value of the figure-of-merit. When the model response closely matches this sensor measurement, the figure-of-merit has a value near its minimum. This occurs when the estimated location is the correct radius from the close sensor. The search will report the location at this radius which may be a significant distance from the actual impact.

A possible way to correct this problem is to scale each value of the diagonal weighting matrix **R** so that each sensor has approximately the same influence on the figure-of-merit. The values of **R** could be scaled by comparing the magnitude of the data of the five sensor in the isolation region.

The identification system successfully identified the impact with noise added to the sensor data. The noise effected the accuracy of the estimated location slightly. The average error in the estimated location was increased by 5% to 10%. The accuracy of the force reconstruction was not greatly effected.

The reconstruction provided a very good estimate of the energy of the impact force. The greatest difference between the recorded and the reconstructed force occurred near the end of the time history. This difference is due to increasing error between

the experimental and model response late in the signal.

Chapter 10

Conclusion

The impact identification system proved to be a very robust and accurate means of identifying the impact on a composite plate. The system was tested with many impacts distributed over the composite plate with both clean and noisy sensor data and with free and clamped boundaries. The system demonstrated the effectiveness of the identification system based on the smoother/filter.

There were key developments that made the identification system applicable to structures.

- The derivation of the governing equation for a composite plate in state space form. This two dimensional solution was extended from a one dimensional beam solution.

- The reformulation of the filter/smoother to handle systems with a large number of degrees of freedom. The reformulation saved considerable computation time in this structures application.

- The use of small circular piezo-electric sensors to measure a non-directional strain property on the surface of the composite plate. These sensors provided a simple and reliable means of measuring the plate response.

Future work could include the application of the identification system to more complicated problems. The forward model can be extended to include more general

structures. Finite element models can also be used. The inverse problem solver based on the smoother/filter, is a very general solution technique and can be applied to other new structures problems.

Appendices

Appendix A

The Observation Matrix

The calculation of the plate deflection and strain, presented in Chapter 5, uses a simplified submatrix $\mathbf{C}_w$, of the observation matrix, $\mathbf{C}$. This simplified matrix is attained by taking advantage of the symmetry of the impact problem.

The equation used to calculate the plate deflection, w, begins with the two-dimensional Fourier Transform between the space and frequency domain:

$$w(x_i, y_j, t) = \sum_{n=0}^{N-1} \sum_{m=0}^{M-1} \bar{w}_{mn}(\kappa_m, \kappa_n, t) e^{i\kappa_m x_i + i\kappa_n y_j} \qquad (A.1)$$

where $\bar{w}_{mn}$ are the frequency components of the plate displacement. $\kappa_m = \frac{2\pi m}{X}$ and $\kappa_n = \frac{2\pi n}{Y}$. M and N are the number of frequency components in the x and y directions. X and Y are the extent of the spatial domain. This equation can be written in matrix form

$$w(x_i, y_i, t) = \mathbf{C}_w \bar{\omega} \qquad (A.2)$$

where $\bar{\omega}$ is a $[N \cdot M \times 1]$ vector with elements

$$\bar{\omega}(n + Nm) = \bar{\omega}_{mn} \qquad (A.3)$$

and $\mathbf{C}_w$ is a $[1 \times M \cdot N]$ vector for each sensor with elements

$$\mathbf{C}_w(n + Nm) = e^{i\kappa_m x_i + i\kappa_n y_j} \qquad (A.4)$$

where $m = 0, \ldots, (M-1)$ and $n = 0, \ldots, (N-1)$.

To better visualize the symmetry of the problem, the matrix $\mathbf{C}_w$ is temporarily presented as a $[M \times N]$ matix.

$$\mathbf{C}_w(nm) = e^{i\kappa_m x_i + i\kappa_n y_j} \tag{A.5}$$

The size of this matrix can be reduced to approximately one quarter of its original size with the symmetric properties of the exponents

$$\begin{aligned} e^{i\kappa(M-m)x_i} &= e^{i\kappa_m x_i} \\ e^{i\kappa(N-n)y_j} &= e^{i\kappa_n y_j} \end{aligned} \tag{A.6}$$

The reduction in the size of the $\mathbf{C}_w$ can be visualized by dividing the matrix into four sections about the $m = \frac{M}{2}$ and $n = \frac{N}{2}$ element. The matrix can then be folded about the x and y divisions. The resulting elements, with the exception of the edge elements, are the addition of the four sections.

The matrix can be further simplified. The displacement of the plate, w, is a real and symmetric function about the x and y axes. The Fourier Transform of a real and even fuction in the space domian results in a real and even fuction in the frequency domain. This means the components of $(\mathbf{C}_w)_{mn}$ are real and symmetric about the $n = \frac{N}{2}$ and $m = \frac{M}{2}$ element. Because of this symmetry and the relation

$$e^{ix} = \cos(x) + i\sin(x) \tag{A.7}$$

the odd function, $i\sin(x)$, will have no contribution when the displacement is calculated. The final simplified $\mathbf{C}_w$ matrix are presented in the vector form.

The middle elements are
$m{=}1{:}(\frac{M}{2} - 1)$, $n{=}1{:}(\frac{N}{2} - 1)$

$$\mathbf{C}_w(n + Nm) = 4e^{i\kappa_m x_i + i\kappa_n y_j} = 4\cos(\kappa_m x_i)\cos(\kappa_n y_j) \tag{A.8}$$

and the edge elements are
$m{=}0$, $n{=}0$

$$\mathbf{C}_w(0) = e^{i0x_i + i0y_j} = 1 \tag{A.9}$$

$m{=}0$, $n{=}1{:}(\frac{N}{2} - 1)$

$$\mathbf{C}_w(n) = 2e^{i0x_i + i\kappa_n y_j} = 2e^{i\kappa_n y_j} = 2\cos(\kappa_n y_j) \tag{A.10}$$

$m=0$, $n=\dfrac{N}{2}$

$$\mathbf{C}_w(\frac{N}{2}) = e^{i0x_i + i\kappa_{\frac{N}{2}} y_j} = e^{i\kappa_{\frac{N}{2}} y_j} = \cos(\kappa_{\frac{N}{2}} y_j) \tag{A.11}$$

$m=\dfrac{M}{2}$, $n=0$

$$\mathbf{C}_w(\frac{N}{2}\frac{M}{2}) = e^{i\kappa_{\frac{M}{2}} x_i + i0y_j} = e^{i\kappa_{\frac{M}{2}} x_i} = \cos(\kappa_{\frac{M}{2}} x_i) \tag{A.12}$$

$m=\dfrac{M}{2}$, $n=1{:}(\dfrac{N}{2} - 1)$

$$\mathbf{C}_w(n + \frac{N}{2}\frac{M}{2}) = 2e^{i\kappa_{\frac{M}{2}} x_i + i\kappa_n y_j} = 2\cos(\kappa_{\frac{M}{2}} x_i)\cos(\kappa_n y_j) \tag{A.13}$$

$m=\dfrac{M}{2}$, $n=\dfrac{N}{2}$

$$\mathbf{C}_w(\frac{N}{2} + \frac{N}{2}\frac{M}{2}) = e^{i\kappa_{\frac{M}{2}} x_i + i\kappa_{\frac{N}{2}} y_j} = \cos(\kappa_{\frac{M}{2}} x_i)\cos(\kappa_{\frac{N}{2}} y_j) \tag{A.14}$$

$m=1{:}(\dfrac{M}{2} - 1)$, $n=0$

$$\mathbf{C}_w(\frac{N}{2}m) = 2e^{i\kappa_m x_i + i0y_j} = 2e^{i\kappa_m x_i} = 2\cos(\kappa_m x_i) \tag{A.15}$$

$m=1{:}(\dfrac{M}{2} - 1)$, $n=\dfrac{N}{2}$

$$\mathbf{C}_w(\frac{N}{2} + \frac{N}{2}m) = 2e^{i\kappa_m x_i + i\kappa_{\frac{N}{2}} y_j} = 2\cos(\kappa_m x_i)\cos(\kappa_{\frac{N}{2}} y_j) \tag{A.16}$$

With these relations, $\mathbf{C}_w$ can be expressed in the simplified vector form in Chapter 5. For $m = 0, \ldots, \frac{M}{2}$ and $n = 0, \ldots, \frac{N}{2}$, each row becomes

$$\mathbf{C}_w =$$
$$
\begin{array}{ccccc}
[& 1 & \cdots & 2\cos(\kappa_n y_j) & \cdots & \cos(\kappa_{N/2} y_j) \\
\cdots & 2\cos(\kappa_m x_i) & \cdots & 4\cos(\kappa_m x_i)\cos(\kappa_n y_j) & \cdots & 2\cos(\kappa_m x_i)\cos(\kappa_{N/2} y_j) \\
\cdots & \cos(\kappa_{M/2} x_i) & \cdots & 2\cos(\kappa_{M/2} x_i)\cos(\kappa_n y_j) & \cdots & \cos(\kappa_{M/2} x_i)\cos(\kappa_{N/2} y_j) &]
\end{array}
$$
$$\tag{A.17}$$

Appendix B

Existing Formulation for Backward Filter

This computational procedure is used by Bryson [11] to solve the smoother equations.

Continuing from the measurement downdate relations Eq. 6.16, the time downdate procedure starts with the boundary conditions

$$\bar{\mathbf{S}}^B(NT) = \mathbf{S}(NT)$$
$$\bar{\lambda}^B(NT) = \mathbf{S}(NT)$$

(B.1)

and results in the optimal estimation $\mathbf{z}(0)$ at $n = 0$ using the boundary condition Eq. 6.10 as

$$\mathbf{z}(0) = \left[\mathbf{S}^{B-1} + \mathbf{S}(0)\right]^{-1}\left[\lambda^B(0) + \mathbf{S}(0)\mathbf{z}(0)\right]$$

(B.2)

With the boundary conditions, we can solve the two point boundary value problem by sweeping forward from $n = 0$. However, the Euler-Lagrange equation is unstable in either direction. A stable sequencing can be done by storing a vector $f^B(n)$ and a matrix $\mathbf{K}^B(n)$ during the backward sequencing

$$\mathbf{K}_B(n) = \mathbf{W}_{ff}^{-1}(NT-n)\mathbf{W}_{zf}^T(NT-n)$$

$$f_B(n) = \mathbf{W}_{ff}^{-1}(NT-n)\mathbf{\Gamma}^T\boldsymbol{\lambda}^B(n+1) \tag{B.3}$$

The forward sequence is then

$$f(n) = f^B(n) - \mathbf{K}^B(n)\mathbf{z}(n)$$

$$\mathbf{s}(n) = \mathbf{C}\mathbf{z}(n) \tag{B.4}$$

$$\mathbf{z}(n+1) = \mathbf{\Phi}\mathbf{z}(n) + \mathbf{\Gamma}f(n)$$

Appendix C

Rank-Two Update Procedure

The outer loop of the inverse problem solver uses the Hessian matrix to update the estimate of the impact location. The impact is updated using the quasi-newton method

$$\mathbf{x}_e(i+1) = \mathbf{x}_e(i) - \alpha \bar{\mathbf{J}}_{xx}^{-1}(i) \bar{\mathbf{J}}_{x_e}(i) \tag{C.1}$$

where $\mathbf{x}_e$ is the estimate of the impact location, and α is the step size scaling variable.

The Hessian matrix, $\bar{\mathbf{J}}_{xx}(i)$, is calculated approximately using a rank-two update precedure. The procedure uses the gradiant information from the current and previous estimates of the impact location. This technique is shown in completion in Cuthbert and Luenberger [14] and [15].

The change in the estimated impact location, p, and the change in the gradiant, q, from one estimated location to the next is

$$\begin{aligned} \mathbf{p}(i) &= \mathbf{x}_e(i+1) - \mathbf{x}_e(i) \\ \mathbf{q}(i) &= \bar{\mathbf{J}}_{x_e}(i+1) - \bar{\mathbf{J}}_{x_e}(i) \end{aligned} \tag{C.2}$$

The update uses two rank-one matrices which are the outer products of the $\mathbf{p}$ and $\mathbf{q}$ matrices. This provides at most a rank-two update.

$$\bar{\mathbf{J}}_{xx}(i+1) \approx \bar{\mathbf{J}}_{xx}(i) + \frac{\mathbf{q}(i)\mathbf{q}^T(i)}{\mathbf{q}^T(i)\mathbf{p}(i)} - \frac{\bar{\mathbf{J}}_{xx}(i)\mathbf{p}(i)\mathbf{p}^T(i)\bar{\mathbf{J}}_{xx}^T(i)}{\mathbf{p}(i)^T\bar{\mathbf{J}}_{xx}^T(i)\mathbf{p}(i)} \tag{C.3}$$

The initial value of the Hessian, $\bar{\mathbf{J}}_{xx}(0)$, can be chosen as any symmetric posititve definite matrix. The identitiy matrix is commonly used causing the first update to

be in the direction of steepest descent.

To provide for easier calculation Eq. C.3 can be inverted directly. The approximation to the inverse Hessian matrix $\mathbf{H}(i)$ can be calculated with

$$
\begin{aligned}
\mathbf{H}(i+1) \;=\;& \mathbf{H}(i) + \left(1 + \frac{\mathbf{q}^T(i)\mathbf{H}(i)\mathbf{q}(i)}{\mathbf{p}^T(i)\mathbf{q}(i)}\right) \frac{\mathbf{p}(i)\mathbf{p}^T(i)}{\mathbf{p}^T(i)\mathbf{q}(i)} \\
&- \frac{1}{\mathbf{p}^T(i)\mathbf{q}(i)} \left(\mathbf{p}(i)\mathbf{q}^T(i)\mathbf{H}(i) + \mathbf{H}(i)\mathbf{q}(i)\mathbf{p}^T(i)\right)
\end{aligned}
\tag{C.4}
$$

Bibliography

[1] E. Wu and J. Yeh, "Identification of impact forces at multiple locations on laminated plates," *AIAA Journal*, vol. 32, no. 12, pp. 2433–2439, 1994.

[2] C. Yen and E. Wu, "On the inverse problem of rectangular plates subjected to elastic impact, part i: Method development and numerical verification," *ASME Journal of Applied Mechanics*, vol. 62, pp. 692–698, September 1995.

[3] C. Yen and E. Wu, "On the inverse problem of rectangular plates subjected to elastic impact, part ii: Experimental verification and further applications," *ASME Journal of Applied Mechanics*, vol. 62, pp. 699–705, September 1995.

[4] J. Shaw, J. Sirkis, E. Friebele, R. Jones, and A. Kersey, "Model of transverse plate impact dynamics for design of impact detection methodologies," *AIAA Journal*, vol. 33, no. 7, pp. 1327–1334, 1995.

[5] R. Jones and J. Sirkis, "Location and magnitude of impact detection in composite plates using neural networks," *SPIE Smart Structures and Materials*, vol. 2444, pp. 469–480, 1995.

[6] M. Gunther, A. Wang, R. Fogg, S. Starr, K. Murphy, and R. Claus, "Fiber optic impact detection and location system embedded in a composite material," *SPIE Smart Structures and Materials*, vol. 1798, pp. 262–269, 1992.

[7] K.Choi and F. Chang, "Identification of impact force and location using distributed sensors," *Jounal of AIAA*, vol. 34, no. 1, pp. 136–142, 1996.

[8] S. Tsai, *Composite Design* . Dayton, Ohio: Think Composite, 1988.

[9] G. F. Franklin, J. Powell, and M. Workman, *Digital Control of Dynamic Systems* . Addison-Wesley, 2nd edition, 1990.

[10] J. Doyle, *Wave Propagation in Structures* . Springer-Verlag, 1989.

[11] A. Bryson and M. Idan, "Parameter identification on linear systems based on smoothing," *Journal of Guidance and Control and Dynamics*, vol. 15, pp. 901–911, July-August 1992.

[12] K. Choi, *An Impact Identification Method Using Distributed Sensor Measurements.* PhD thesis, Department of Aeronautics and Astronautics, Stanford University, 1993.

[13] A. P. Sage and J. L. Melsa, *System Identification.* New York and London: Academic Press, 1971.

[14] T. Cuthbert, *Optimization Using Personal Computers with Application to Electrical Networks.* New York: Wiley, 1987.

[15] D. Luenberger, *Linear and Nonlinear Programming.* Reading MA: Addison-Wesley, 2nd edition, 1984.